Editors' Suggestion

Thermodynamic insights into the intricate magnetic phase diagram of $EuAl_4$

William R. Meier,[1,*] James R. Torres,[1,†] Raphael P. Hermann,[1] Jiyong Zhao,[2] Barbara Lavina,[2,3] Brian C. Sales,[1] and Andrew F. May[1,‡]

[1]*Materials Science & Technology Division, Oak Ridge National Laboratory, Oak Ridge, Tennessee 37831, USA*
[2]*Advanced Photon Source, Argonne National Laboratory, 9700 S. Cass Avenue, Argonne, Illinois 60439, USA*
[3]*Center for Advanced Radiation Sources, The University of Chicago, Chicago, Illinois 60637, USA*

(Received 5 April 2022; accepted 31 August 2022; published 19 September 2022)

The tetragonal intermetallic compound $EuAl_4$ hosts an exciting variety of low-temperature phases. In addition to a charge density wave below 140 K, four ordered magnetic phases are observed below 15.4 K in zero field. Recently, a skyrmion phase was proposed based on Hall effect measurements under a *c*-axis magnetic field. We present a detailed investigation of the phase transitions in $EuAl_4$ under *c*-axis magnetic field. Our dilatometry, heat-capacity, DC magnetometry, AC magnetic susceptibility, and resonant ultrasound spectroscopy measurements reveal three magnetic phase transitions not previously reported. The first key result is a detailed $\boldsymbol{H} \parallel [001]$ magnetic phase diagram mapping the seven phases we observe. Second, we identify a high-field phase, phase VII, which directly corresponds to the region were skyrmions have been previously suggested. Our results provide guidance for future studies exploring the complex magnetic interactions and spin structures in $EuAl_4$.

DOI: 10.1103/PhysRevB.106.094421

I. INTRODUCTION

Topological spin textures, such as skyrmions and merons, have generated significant interest for their promise for next-generation electronic devices [1–3]. These phases are characterized by patterns of swirling magnetic moments built from superimposed, incommensurate magnetic modulation (multi-Q order). The resulting moment configuration gives rise to a topological Hall effect, a critical signal for identifying candidate materials.

Two routes to topological magnetic textures have been identified in bulk materials. Originally, transition metal compounds without inversion symmetry (noncentrosymmetric) were explored. In these materials, a Dzyaloshinskii-Moriya interaction can promote the swirling noncoplanar magnetic configurations [1,3]. An alternative route has been proposed in centrosymmetric materials. In these systems, noncoplanar magnetic textures arise from lattice frustration, higher-order interactions, or competition between nearest- and next-nearest-neighbor interactions [1,4–8]. In metallic rare-earth systems like Gd_2PdSi_3, $Gd_3Ru_4Al_{12}$, and $GdRu_2Si_2$, the Ruderman-Kittel-Kasuya-Yosida (RKKY) interaction is proposed to provide the competing couplings [9–15]. These systems have attracted attention because the smaller size of the skyrmions textures could allow for significantly smaller devices and they also yield enhanced electronic signatures [1].

Now we will introduce the skyrmion candidate $EuAl_4$ and its intricate low-temperature behavior. This tetragonal compound crystallizes with the $BaAl_4/ThCr_2Si_2$ structure type ($I4/mmm$ No. 139). This centrosymmetric structure [Fig. 1(d)] is composed of square Eu nets separated by corrugated [16] Al sheets. Members of the $BaAl_4$ family include MAl_4 and MGa_4 with M = Ca, Sr, Ba, and Eu. All are excellent metals [17–19].

The zero-field behavior of $EuAl_4$ is summarized in Fig. 1 [18,20]. Five transitions are observed in $EuAl_4$ below room temperature [Fig. 1(a)]. Below T_{CDW}, around 140 K, a charge-density-wave (CDW) modulation appears [18–21]. $SrAl_4$ also hosts a CDW [17]. Shimomura *et al.* made a detailed x-ray diffraction study of this lattice modulation in $EuAl_4$ and identified a modulation wave vector of $(0, 0, 0.18)$ rlu [22]. More recent analysis of single-crystal data by Ramakrishnan *et al.* suggests that an orthorhombic CDW phase is likely [21]. Despite broken tetragonal symmetry below T_{CDW}, associated peak splitting was not observed by either diffraction study. Shimomura *et al.* observed distinct breaking of tetragonal symmetry below roughly 12 K (around T_{N3}). In this low-temperature range [left box in Fig. 1(b)] a and b differ by $>0.1\%$.

Next, we introduce the magnetic phases in $EuAl_4$ [summarized in Fig. 1(c)]. Europium in this compound is divalent [17,23] and therefore possesses an essentially spin-only magnetic moment ($S = \frac{7}{2}$). Antiferromagnetic order develops at $T_N = 15.4$ K followed by three additional magnetic transitions on cooling [17,18,24]. Roman numerals are used throughout this paper to label the numerous magnetic phases.

*Current Address: Materials Science & Engineering Department, University of Tennessee Knoxville, Knoxville, Tennessee 37996, USA; javamocham@gmail.com
†Current Address: Materials Science and Technology Division, Los Alamos National Laboratory, Los Alamos NM 87545, USA.
‡mayaf@ornl.gov

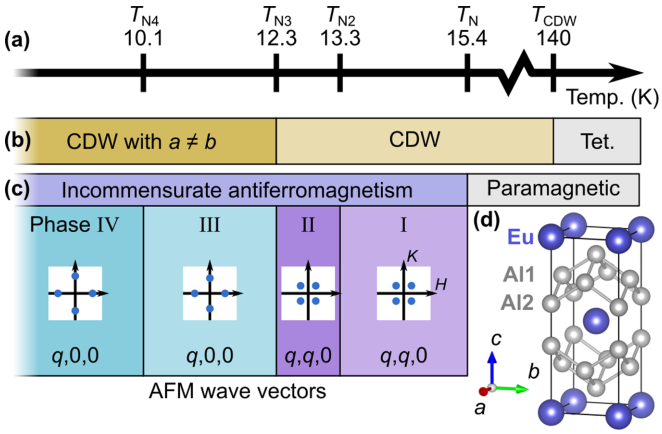

FIG. 1. Summary of low-temperature phases in $EuAl_4$. (a) Phase transition temperatures. (b) Progression of crystal structures. (c) The four zero-field magnetic phases and their roman numeral labels. The antiferromagnetic propagation vectors determined by Kaneko *et al.* [25] for each phase are depicted as spots in the $HK0$ plane with the form of the wave vectors below. It is unknown if any of these phases have multi-Q magnetic order. (d) Room-temperature structure of $EuAl_4$ rendered in VESTA [16].

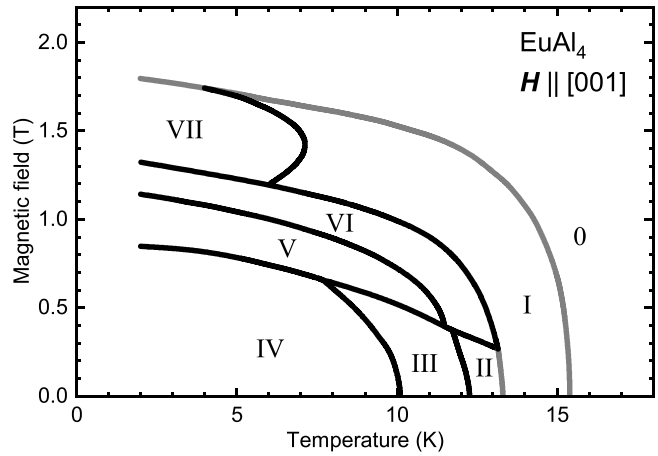

FIG. 2. Schematic phase diagram of magnetic phases in $EuAl_4$ for c-axis magnetic field determined in this study. The magnetic fields reported in this paper are the applied field without a demagnetization correction (see Appendix B). Phase fields are labeled with roman numerals. Phase 0 is the paramagnetic or field-polarized phase with the CDW modulation. Black and gray lines represent phase boundaries we believe are discontinuous and continuous, respectively. The I-VII, II-VI, and III-V phase boundaries are the phase transitions proposed in this study.

The neutron diffraction study by Kaneko *et al.* revealed that the four zero-field phases host incommensurate magnetic order [25]. As depicted in Fig. 1(c), both phases I and II host incommensurate modulations with propagation vectors $(q, q, 0)$ and $(q, -q, 0)$. Below $T_{N3} = 12.3$ K a different incommensurate magnetic order is present. In phases III and IV the magnetic diffraction peaks were indexed to $(q, 0, 0)$ and $(0, q, 0)$. The temperature dependence of the CDW in Ref. [22] shows clear competition between the $(q, 0, 0)$ magnetic order and the CDW modulation. Finally, it is not clear if any of these phases have multi-Q magnetic order.

The evolution of the four antiferromagnetic phases with magnetic field was examined in Ref. [18]. They report a curious series of metamagnetic transitions with increasing field along the [001] direction. Subsequently, Shang *et al.* reported that the last phase before the field-polarized phase had an additional Hall contribution they suggested could be a topological contribution from a skyrmion phase [24]. A temperature-field region with a similar Hall signal was observed in $EuGa_4$ and $EuGa_2Al_2$ [26,27]. These phases with unusual Hall effects are reminiscent of the topological Hall phase observed in $GdRu_2Si_2$, which shares the same structure type and spin-$\frac{7}{2}$ moment [11]. In this case, the Hall contribution was determined to arise from a skyrmion or meron [14] phase.

In this paper we provide thermodynamic insights into the intricate magnetic phase diagram of $EuAl_4$ under c-axis magnetic field ($\boldsymbol{H} \parallel [001]$). The most important product of our investigation is a revised phase diagram for $EuAl_4$ (depicted in Fig. 2). We clearly identify seven magnetic phases labeled with roman numerals. We also present evidence for which transitions are discontinuous and continuous (black and gray lines in Fig. 2, respectively). The subtle, discontinuous I-VII transition is particularly significant. Phase VII corresponds to the T, H region where the topological Hall effect is reported in Ref. [24]. The data presented here do not preclude skrymion or meron formation in phase VII. Our detailed phase diagram and insights into the individual phases will guide future investigations to uncover details of the interactions that lead to the rich magnetic behavior of $EuAl_4$.

The paper is organized as follows. First, in Sec. II we describe how we obtained and characterized the $EuAl_4$ single crystals. In Sec. III we present our dilatometry, heat-capacity, DC magnetization, AC magnetic susceptibility, and resonant ultrasound spectroscopy results. We examine the characteristic signatures of the CDW transition and zero-field magnetic phases in Secs. III A and III B. In total, we identify seven magnetic phases in the $\boldsymbol{H} \parallel [001]$ phase diagram (Fig. 2). In Sec. IV we discuss the characteristics of these phases in greater detail. Multi-Q skyrmion and meron crystals are closely tied to the tetragonal symmetry [14]. In Sec. IV A we discuss which phases show strong distortions from tetragonal symmetry. In Sec. IV B we explore the character of the magnetic phases and transitions in light of our thermodynamic measurements. Next, we discuss what we know about the intriguing phase VII (Sec. IV C). Finally, we discuss future directions of investigation in $EuAl_4$ (Sec. IV D).

II. METHODS

A. Growth

$EuAl_4$ crystals were grown from a high-temperature aluminum-rich melt, as in previous works [18,19,28–30]. We roughly followed the method from Nakamura *et al.* starting with a Eu:Al = 1:9 atomic ratio [18]. Eu pieces (Ames Laboratory, Materials Preparation Center 99.99+%) and Al shot (Alfa Aesar 99.999%) totaling 2.5 g were loaded into one side of a 2-mL alumina Canfield Crucible Set [31]. The crucible set was sealed under $\frac{1}{3}$ atm argon in a fused silica ampoule.

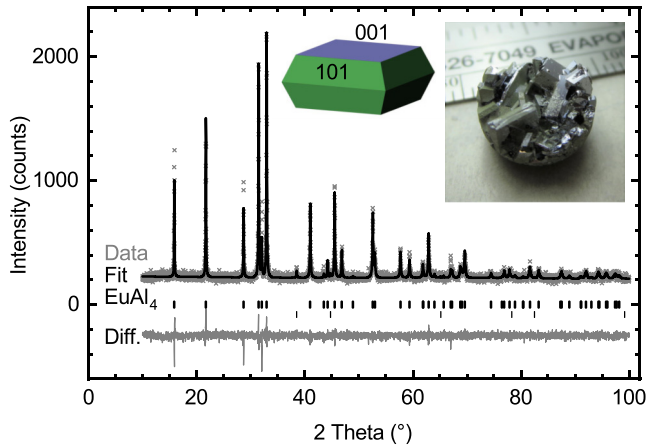

FIG. 3. Powder x-ray diffraction pattern from ground $EuAl_4$ crystals. Rietveld refinement estimates majority $EuAl_4$ and about 3 wt.% Al metal (upper and lower rows of ticks, respectively). The middle inset depicts the observed to-go box crystal form rendered in JCrystal [32] with labeled faces. The right inset is a photo of an attractive cluster of metallic $EuAl_4$ exemplifying their well-faceted, tabular habit. A millimeter scale sits behind.

The ampoule assembly was placed in a box furnace and heated to 900 °C over 6 h (150 °C/h) and held for 12 h to melt and homogenize the metals. Crystals were precipitated from the melt during a slow cool to 700 °C over 100 h (−2 °C/h). To liberate the crystals from the remaining liquid, the hot ampoule was removed from the furnace, inverted into a centrifuge, and spun.

B. Products

The right-hand inset in Fig. 3 shows a cluster of $EuAl_4$ crystals obtained from this procedure. They look very similar to those of other $BaAl_4$-type aluminides [17,19]. These silver-metallic crystals ranged from rounded, anhedral submillimeter grains up to blocky or tabular crystals 6 mm wide and 2 mm thick. These faceted grains adopted a square bifrustum shape (center inset of Fig. 3) [32] with rectangular basal (001) faces and trapezoidal {101} faces (determined by x-ray diffraction).

Clean crystals had mirrorlike faces but many grains were coated in residual soft aluminum metal covered with a yellow-green phase that we suspect to be Eu oxides or hydroxides. Most aluminum metal could be removed by an overnight soak in 0.6 M HCl or a 1.2 M HNO_3 aqueous solution, but the crusty material remained. $EuAl_4$ was not visibly attacked by these acid solutions. The secondary phases were removed when crystals were polished to shape for our experimental investigations. These brittle crystals exhibit conchoidal fracture and are stable in air for many months.

Room-temperature powder x-ray diffraction on ground crystals was performed using a PANalytical X'pert Pro diffractometer equipped with a Cu $K\alpha$ tube and an incident beam monochromator. FULLPROF was used for Rietveld refinement of the pattern (Fig. 3). The dominant phase was $EuAl_4$ with the $BaAl_4/ThCr_2Si_2$ structure type [Fig. 1(d)] with 3 wt.% aluminum metal from the crystal surfaces. The refined structural parameters are consistent with those in previous works [18,29,30,33]: $a = 4.39860(12)$ Å, $c = 11.1740(4)$ Å, and Al2 $z = 0.3874(5)$.

C. Measurements

One $EuAl_4$ crystal was carefully shaped into a rectangular prism for dilatometry. The dimensions were $2.01 \times 1.06 \times 0.72$ mm^3 along the [100], [010], and [001] directions, respectively. Demagnetization effects can frustrate comparison of measurements on different shaped samples (Appendix B). Therefore, we used this same crystal for subsequent magnetometry and heat-capacity measurements to mitigate this issue. We report the applied magnetic fields throughout this paper to avoid some of the artifacts that demagnetization corrections can produce.

Dilatometry measurements were obtained using the Quantum Design dilatometer option [34] in a Quantum Design PPMS DynaCool system. The sample was mounted with magnetic field along the [001] direction monitoring the length change along [100]. Dilation vs temperature was measured on cooling from 360 to 2 K at 12 mK/s. Detailed low-temperature thermal expansion data were obtained on warming and cooling between 2 and 20 K at 5 mK/s under constant applied fields up to 4 T. Dilation vs field data were obtained at constant temperatures from 2 to 18 K by ramping field at 1 mT/s between 0 and 3 T.

Specific-heat capacity (C_p) data were obtained with the heat-capacity option on the same PPMS DynaCool system. The dilatometry sample was mounted on the platform with Apiezon N grease with magnetic field along the [001] direction. Heat capacity was measured using both a standard 2% temperature rise and the "large-pulse" method with a 20% rise. Postprocessing the raw data from the latter method in Quantum Design Multiview software allows us to obtain densely spaced $C_p(T)$ data as the sample warms and cools using the single-slope option. This procedure allows us to capture the evolution of the closely spaced discontinuous transitions in $EuAl_4$ with temperature and field. Most of the data presented in this paper were obtained with the long-pulse method, but C_p values are very consistent with the standard method at temperatures away from phase transitions [see Fig. 5(c)].

Magnetometry measurements were carried out in a Quantum Design MPMS3 system with field along the the c axis. The dilatometry crystal was mounted to a fused silica rod with GE varnish with field along [001]. DC magnetization vs temperature data were measured in constant field up to 2.2 T between 2 and 25 K with a rate of 5 mK/s. This means that temperature sweeps in magnetometry and dilatometry are directly comparable. DC magnetization vs field data were measured at constant temperatures between 2 and 18 K by stabilizing at each field up to 2.5 T. AC magnetometry was also carried out in the MPMS3 using a 257.67-Hz, 0.5-mT drive field. Temperature-dependent data were obtained on cooling from 20 to 2 K at 1.7 mK/s at constant fields up to 2 T.

Resonant ultrasound spectroscopy (RUS) measurements were performed as a function of temperature and applied magnetic field using a custom-built RUS probe compatible with the Quantum Design PPMS. The Alamo Creek Engineering

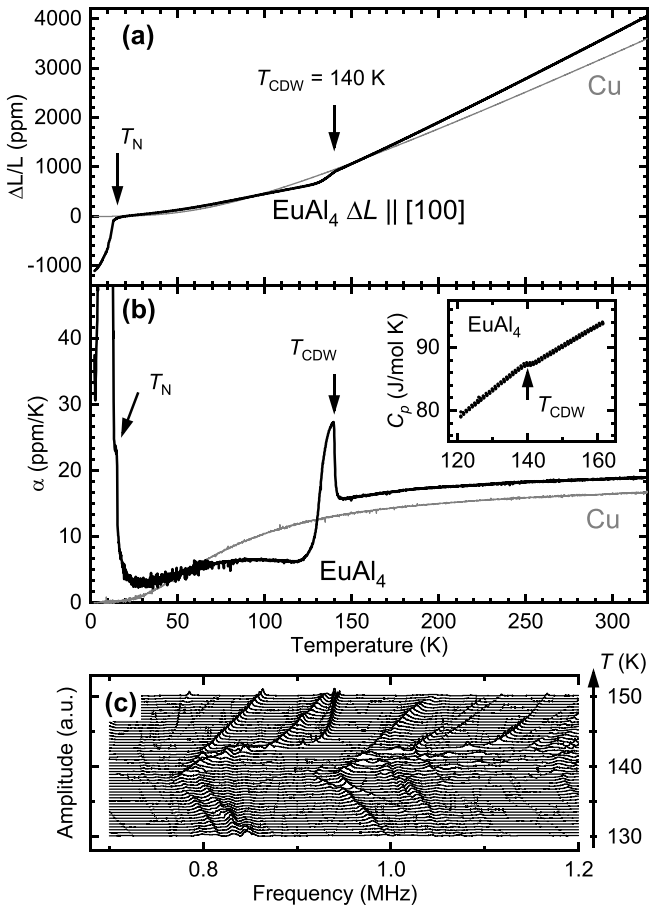

FIG. 4. Thermodynamic signatures of the charge-density-wave (CDW) transition in $EuAl_4$. (a) The thermal expansion $\Delta L/L$ of $EuAl_4$ and copper metal measured on cooling. (b) The coefficient of thermal expansion (α) for $EuAl_4$ and copper metal. The inset shows the specific-heat capacity jump at T_{CDW} consistent with a continuous phase transition. (c) Resonant ultrasound spectroscopy spectra at temperatures spanning the CDW transition measured on warming. Peaks reflect mechanical resonances of the sample.

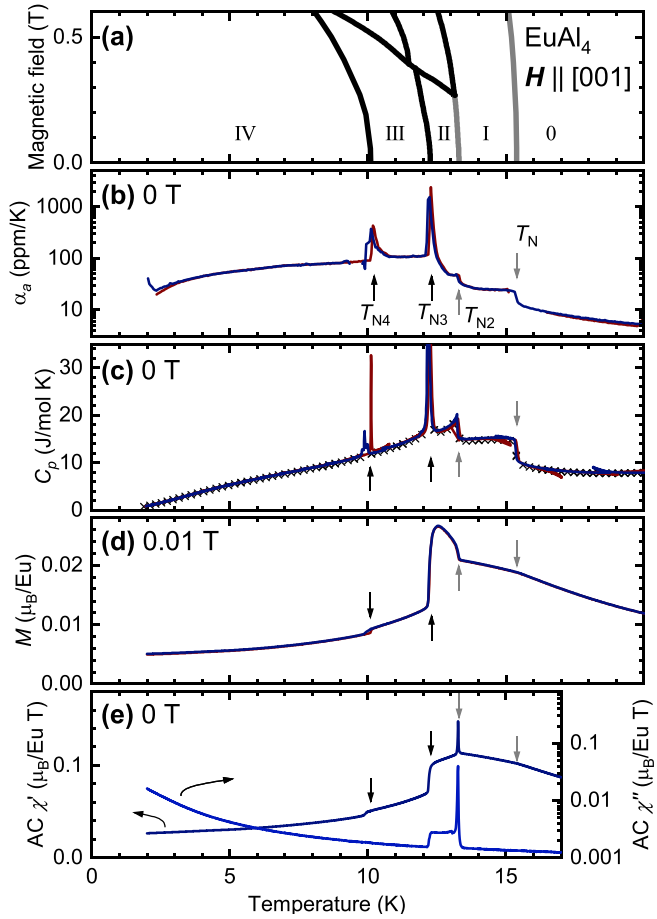

FIG. 5. Zero-field magnetic phases of $EuAl_4$. (a) Low-field section of the phase diagram showing labeled phase fields. (b) Thermal expansion coefficient $\alpha_a(T)$ measured on heating (red) and cooling (blue) showing all four transitions. (c) Zero-field heat-capacity data. Red and blue curves are continuous heat-capacity data derived from the heating and cooling parts of the long-pulse heat-capacity measurement (see Sec. II C). ×'s are heat-capacity values from the standard heat-capacity measurement demonstrating nice agreement with the long-pulse data. (d) DC magnetization measurement along [001] at 0.01 T showing all four transitions on heating (red) and cooling (blue). (e) AC magnetic susceptibility data taken on cooling at zero field. The in-phase (χ') and out-of-phase (χ'') parts are presented in dark and light blue.

(ACE) RUS008 system [35] was used for signal generation and detection, driven by a homemade Python implementation of the ACE software. The $EuAl_4$ sample was approximately rectangular parallelepiped shaped with nominal dimensions $1.292 \times 1.902 \times 0.745$ mm^3 (short length along the [001] direction). A general measurement scheme was employed for all temperature- and applied-field-dependent measurements: frequency scans were recorded continuously over the 0.7–1.2 MHz range with a step size of 20 Hz and dwell time of 4 ms. Temperature and field were ramped continuously at 3.3 mK/s and 0.2 mT/s, respectively; thus, each RUS scan spanned ranges of about 0.3 K and 20 mT, respectively.

^{151}Eu Mössbauer spectra were collected between 20 and 170 K on a 95-mg/cm^2 powder sample of $EuAl_4$ using a 50-mCi $^{151}SmF_3$ source at ambient temperature. The sample was placed in a Janis SHI-850 closed-cycle cryostat. A Wissel GmbH drive in constant acceleration mode was used in the ±30 mm/s range and calibrated by measuring a room-temperature spectrum of α iron. The isomer shift is reported relative to the $^{151}SmF_3$ source. A Tl@NaI scintillator (Ametek) was used as detector.

^{151}Eu nuclear resonant inelastic x-ray scattering (NRIXS) spectra using 21.54-keV synchrotron radiation [36] were measured at the 3-ID beamline of the Advanced Photon Source, Argonne National Laboratory, with 0.8-meV resolution. NRIXS measures the phonon-assisted nuclear resonant absorption of radiation which yields the partial vibrational inelastic scattering function $S(E)$ for the resonant element. The scattering function is directionally projected on the direction of the incident beam in case of measurements on a single crystal [37]. Here, we have utilized two, roughly 100-μm sized, single crystals of $EuAl_4$, respectively oriented with the beam parallel and perpendicular to the a axis. The crystals were glued on a diamond and placed in a miniature cryostat described in Ref. [38].

III. RESULTS

In this section we will present thermodynamic data revealing the numerous phase transitions in $EuAl_4$. We not only observe the previously identified charge density wave (Sec. III A) and four zero-field magnetic transitions (Sec. III B) but also three transitions not observed previously (Secs. III C and III D). We note that only select magnetization data are presented here, but a large number of fields and temperatures were examined to produce the points utilized to draw smooth lines in the presented phase diagrams. Phase diagrams containing these points are shown at the end of this section.

A. Charge density wave

Previous investigations of $EuAl_4$ have observed a charge density wave (CDW) below about 140 K [18,21,22,25,27]. Figure 4 presents thermodynamic signatures of this transition. In Fig. 4(a) we present the thermal expansion $EuAl_4$ along the [100] direction compared to polycrystalline copper. Plots of the thermal expansion coefficient vs temperature of both metals, $\alpha(T) = \frac{1}{L_0}\frac{dL}{dT}$, are presented in Fig. 4(b). Although the length change of $EuAl_4$ is comparable to Cu down to 150 K, it shows dramatic features below this temperature. The CDW transition is marked by a kink in Fig. 4(a) and a steplike increase in α_a by 73% on cooling through $T_{CDW} = 140$ K (indicated by the arrow). A step in $\alpha_a(T)$ is characteristic of a continuous phase transition. Cooling below this transition, α_a smoothly falls to a value 60% smaller than just above T_{CDW}. $EuAl_4$ shows dramatic changes in length below the magnetic ordering temperature T_N. Below this temperature $\alpha_a(T)$ rises steeply. We examine this low-temperature behavior in more detail in Sec. III B.

The inset of Fig. 4(b) presents the specific-heat capacity of $EuAl_4$ across the CDW transition. The steplike feature corroborates the continuous character of the CDW transition identified in thermal expansion.

Resonant ultrasound spectroscopy (RUS) measurements also observe a clear signature of the CDW transition. Figure 4(c) presents a series of RUS spectra at a range of temperatures spanning T_{CDW} on warming. Mechanical resonance modes of the $EuAl_4$ sample give a larger vibration amplitude near the resonant frequency, observed as peaks in each spectrum. Note that in the ultrasound amplitude, resonances can appear as peaks or antipeaks depending on their phase. The resonant frequencies shift as the elastic moduli evolve with temperature. Critically, when moduli stiffen, the resonant frequencies increase and peaks shift to the right, and vice versa.

In Fig. 4(c), note that peaks in the spectra move to lower frequencies as we approach $T_{CDW} = 140$ K from above. In crossing T_{CDW}, the ultrasound signal is modulated significantly, including an even stronger shift toward lower frequencies (softening). Below T_{CDW} we observe the opposite trend: peak frequencies increase on cooling (hardening). This indicates that the elastic modes of the crystal are softening on cooling toward CDW transition and stiffening again below. This evolution of elasticity reflects the coupling of the CDW to the bulk elastic modes. In addition, most of the resonant modes evolve continuously through T_{CDW}, suggesting that T_{CDW} is a continuous transition because we observe an abrupt change in slope of the elastic moduli vs temperature [39].

We observed the CDW superlattice peaks using single-crystal x-ray diffraction at 100 K but we do not present it here. We indexed these with a wave vector of [0 0 0.1822(15)] r.l.u., in good agreement with previous x-ray [22,27] and neutron [25] studies.

We do not observe a signature of the CDW transition in the ^{151}Eu Mössbauer spectral parameters within experimental error bars (Appendix D). This result suggests that the CDW modulation has a more significant impact the Al sublattice rather than the Eu sublattice. To this point, NRIXS does offer a clue about the Eu atoms in the CDW phase. Below T_{CDW}, the Eu atoms show 30% larger atomic displacement parameters along c than in the ab plane (Appendix D). Near room temperature, the dynamic displacement parameters are more isotropic. This likely reflects a change from dynamic displacements of Eu perpendicular to [001] above T_{CDW}, to static displacements in the CDW phase.

Our thermodynamic data show clear indications of the CDW transition observed in previous studies [18,21,22,25,27]. In addition, we provide evidence that the transition is continuous. Finally, we observe that the CDW order has a significant impact on the lattice thermal expansion and elasticity.

B. Magnetic transitions in zero field

Here, we will examine the succession of magnetic orders at low temperature in zero magnetic field. As mentioned in the Introduction, $EuAl_4$ undergoes four magnetic transitions on cooling in zero field (Fig. 1). We observe all four in our thermodynamic measurements shown in Fig. 5. Figure 5(a) depicts the phase transitions of $EuAl_4$ under small magnetic fields along [001] for context.

Figure 5(b) presents the low-temperature [100] coefficient of thermal expansion (α_a) on warming and cooling (red and blue, respectively). First, note the humongous values of α_a within the phases below T_N, ranging from 20 to 100 ppm/K. This is dramatically larger than Cu or Al with α's of 0.001 to 0.3 ppm/K within this temperature range [40]. T_N and T_{N2} are evident as steps in $\alpha_a(T)$ marked by gray arrows. These are suggestive of continuous transitions. In addition, large peaks in $\alpha_a(T)$ appear at $T_{N3} = 12.3$ K and $T_{N4} = 10.1$ K indicative of discontinuous phase transitions. Shimomura *et al.* observed tetragonal symmetry breaking at T_{N3} which accounts for the large strain we observe [22]. We will discuss the symmetry implication of these large strains in Sec. IV A. Clearly, magnetic order is strongly coupled to lattice strain.

The low-temperature heat capacity of $EuAl_4$ is presented in Fig. 5(c). Our $C_p(T)$ data are in excellent quantitative agreement with those presented in Ref. [18]. The features in the heat-capacity data closely track the features of the thermal expansion plot with steps at T_N and T_{N2} and peaks at T_{N3} and T_{N4} once again marked by arrows.

Next, we will consider the DC magnetization data in Fig. 5(d). This was measured at a small field (0.01 T) to obtain an estimate of the zero-field magnetic susceptibility. Magnetization rises on cooling to T_N which is marked by

a slope change. There is an abrupt increase at T_{N2} with an elevated value of M in phase II down to T_{N3} (also observed at the same field in Ref. [24]). Both T_{N3} and T_{N4} are characterized by drops in magnetization on cooling. Data taken on warming and cooling (red and blue, respectively) are nearly identical with only a weak hysteresis visible at T_{N4}.

AC magnetic susceptibility (measured on cooling) tells a subtly different story [Fig. 5(e)]. The in-phase susceptibility $\chi'(T)$ has slope changes at T_N and T_{N2} and steps T_{N3} and T_{N4}. Curiously, there is a discrepancy between the AC and DC susceptibility in phase II. $M(T)$ shows a rounded, negatively sloped plateau in this regime whereas $\chi'(T)$ shows a sharp peak at T_{N2} and a positive sloped region just below. The imaginary part of the AC susceptibility [$\chi''(T)$] also shows different behavior in phase II with a sharp peak at T_{N2} and a flat topped plateau down to T_{N3}. We will examine the discrepancy between the DC and AC magnetic data in phase II in Sec. IV B 1. The $\chi'(T)$ features at T_{N3} and T_{N4} mirror the features observed in $M(T)$ suggestive of discontinuous transitions.

We clearly detect the four previously reported magnetic transitions in $EuAl_4$ at zero field. The Néel transition (T_N) has continuous character in all the measurements. The nature of the transition at T_{N2} is less clear (see Sec. IV B 1). T_{N3} and T_{N4} are both clearly discontinuous transitions indicated by the peaks in $\alpha_c(T)$ and $C_p(T)$ and steps in $M(T)$ and have a thermal hysteresis of about 0.1 K. These designations are consistent with previous data on $EuAl_4$ [18,24].

C. Magnetic transitions at low field

We now turn our attention to the magnetic phases in $EuAl_4$ at low magnetic fields. Within this regime, we observe transitions between 0.3 and 0.5 T not previously reported. Figures 6 and 7 present our evidence for transitions between phases II and VI and phases III and V.

Figure 6 presents thermodynamic measurements at 0.5 T showing evidence for the transition between phases III and V centered at 10.3 K. We observe five transitions in the thermal expansion, heat-capacity, and DC magnetization measurements [Figs. 6(b)–6(d)] at this field (marked with arrows). The horizontal dashed line in Fig. 6(a) places these transitions in context of the phase diagram. At this field, only the magnetic ordering transition, T_N, has continuous character as evidenced by steps in $\alpha_c(T)$, $C_p(T)$, and $\frac{dM}{dT}(T)$.

For fields below 0.2 T, the transition at T_{N2} has predominant continuous character (see Fig. 5). At higher fields, the transition takes on discontinuous character like that at 12.8 K in 0.5-T plots (Figs. 6(b)–6(d)]. This change coincides with the triple point between phases I, II, and VI. Further evidence for the two distinct phase fields for phases II to VI and the transition between them will be presented later in this section.

At lower temperatures, there are three additional discontinuous transitions at 11.3, 10.3, and near 8.7 K in our 0.5-T data sets. These appear as peaks in $\alpha_c(T)$, $C_p(T)$, and $\frac{dM}{dT}(T)$. The transition between phases III and V at 10.3-K transitions stands out here as unusually broad in all three measurements (see Sec. IV B 3). Despite this, the transition has limited thermal hysteresis. This feature also appears in the field-dependent data in Fig. 7 discussed below. The lowest-temperature III-IV transition at 0.5 T has a relatively strong thermal hysteresis of about 0.2 K just like the corresponding transition at zero field, T_{N4}.

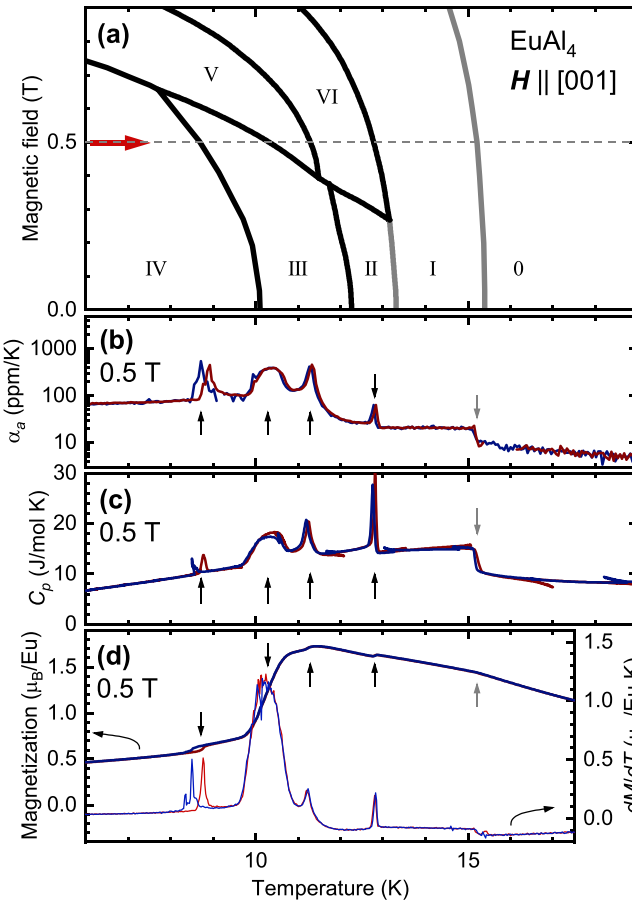

FIG. 6. Additional low-field III-V transition evident $\mu_0 H = 0.5$ T measurements. (a) Cropped phase diagram showing the phase fields in the region of interest. The arrow and horizontal dashed line place the measurements in context. (b) [100] thermal expansion data of $EuAl_4$ at 0.5 T taken on warming (red) and cooling (blue). Five transitions are observed and marked with arrows. Note the logarithm scale. (c) Heat-capacity data obtained at 0.5 T using the long-pulse method. Red and blue curves represent C_p values obtained from the warming and cooling parts of each pulse, respectively. (d) DC magnetization data (thicker curves) clearly revealing all five transitions on warming and cooling. The temperature derivatives $\frac{dM}{dT}(T)$ are presented as thinner lines with the right-hand axis.

Figure 7 provides further evidence of the low-field transitions. Figure 7(a) depicts four isothermal sections through the phase diagram. Field-dependent DC magnetization and a-axis dilation data are presented on the right for each temperature [Figs. 7(b)–7(e) and 7(f)–7(i), respectively). Thinner lines represent the field derivatives of quantities $\frac{dM}{d(\mu_0 H)}$ and the magnetostriction coefficient $\lambda_a = \frac{1}{L_0}\frac{dL}{d(\mu_0 H)}$. Note that the phase boundaries in the phase diagram in Fig. 7(a) are reflected in the distinctive features in the field-dependent data to the right marked with arrows.

First we will consider how the III-IV phase boundary appears in these field-dependent data. At 9 K, the first transition

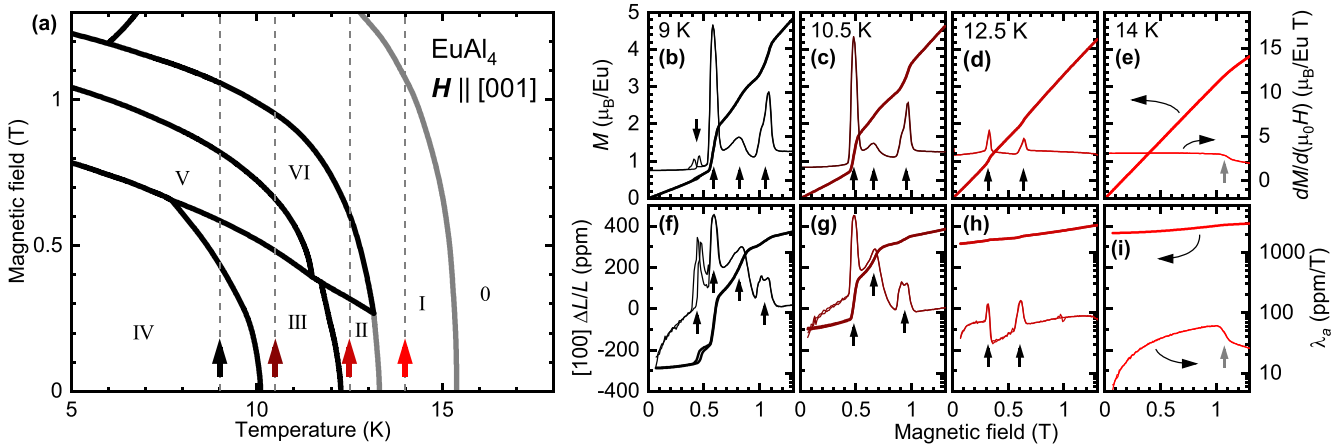

FIG. 7. Evidence for low-field phase transitions in field-dependent measurements. (a) Phase diagram showing the labeled phase fields. The arrows and vertical dashed lines reveal the isothermal cuts that correspond to the magnetic and dilation data on the right. (b)–(e) Thick and thin curves represent the field dependence of magnetization M and its derivative $\frac{dM}{d(\mu_0 H)}$ at four temperatures. Black and gray arrows denote the discontinuous and continuous transitions. (f)-(i) Thick and thin curves present the dilation ($\frac{\Delta L}{L}$) and magnetostriction coefficient (λ_a) as a function of field, respectively. Note that curves for both increasing and decreasing field are plotted in (b)–(i). Only the III-IV transition at 0.43 T in the 9-K plots show any significant hysteresis.

appears as a hysteretic jump around 0.43 T in the magnetization and dilation plots (as well as peaks in their derivatives). This feature is the continuation of the discontinuous T_{N4} transition observed in Figs. 5 and 6. As in those cases, the transition shows relatively strong hysteresis.

Next, we turn to the III-V phase transition observed at 10.3 K in Fig. 6. It is clearly observed in the 9- and 10.5-K data at 0.59 and 0.48 T in Fig. 7, respectively. On increasing field, the transition manifests as a strong step up in $M(\mu_0 H)$ and a significant extension of the crystal (1.2 μ_B/Eu and 250 ppm at 9 K, respectively). These dramatic changes in thermodynamic properties in Figs. 6 and 7 clearly suggest that phases III and V are distinct phases separated by a discontinuous transition. Section IV B 3 provides a deeper discussion of this phase transition.

At higher fields, we can see the signature of the transition between phases V and VI. The transition appears in the 9- and 10.5-K field-dependent data as broad steeper region in the magnetization and dilation curves centered at 0.82 and 0.66 T, respectively. We suspect that the V-VI transition is discontinuous based on its character in temperature-dependent measurements. In particular, the peaks observed in $\alpha_a(T)$, $C_p(T)$, and $\frac{dM}{dT}(T)$ in Fig. 6 clearly suggest a discontinuous transition.

The I-VI phase boundary appears in phase diagrams already reported [18,24]. In addition to the feature at 12.8 K in Fig. 6, we observe the I-VI transition in our field-dependent results in Fig. 7. Note the steps at 1.05, 0.95, and 0.64 T in our $M(\mu_0 H)$ and $\Delta L/L$ plots measured at 9, 10.5, and 12.5 K, respectively. Curiously, $\frac{dM}{d(\mu_0 H)}$ and λ_a reveal double peaks at this field at the lower two temperatures. This is particularly evident in the dilatometry results [Figs. 7(f) and 7(g)] and AC susceptibility measurement (not shown) and is discussed in greater detail in Sec. IV B 4.

In addition to the III-V phase boundary we propose above, our results also reveal a transition around 0.35 T between phases II and VI. The field-dependent data at 12.5 K in Fig. 7(d) show a subtle jump of magnetization and sample length at 0.32 T. This produces a sharp peak in $\frac{dM}{d(\mu_0 H)}$ and λ_a plots with no obvious hysteresis. In addition to this feature, we also observe a change in the magnetostriction coefficient across the boundary; λ_a falls from 70 ppm/T in phase II to 34 ppm/T in phase VI. As we noted above, there is also a change from continuous I-II phase boundary to discontinuous in the I-VI boundary within this field range. This all points to phases II and VI being distinct phases separated by previously unreported transition near 0.35 T. See Sec. IV B 3 for more details.

Finally, we observe the transition between phase I and the paramagnetic/field-polarized phase 0, as evident from the change in slope $M(\mu_0 H)$ and $\Delta L/L$ indicating continuous character at all temperatures. Within the field range presented, we only see this feature in the 14-K data [Figs. 7(e) and 7(i)] and is most easily seen as a step in the field derivatives at 1.07 T.

D. Magnetic transitions at high field

In addition to the transitions evidenced in the previous section, we identify an additional phase in $EuAl_4$ just below the saturation field. This phase VII region is important because this is the regime where a topological Hall contribution is proposed by Shang *et al.* [24].

Figure 8 depicts the extent of phase VII in $EuAl_4$ and evidence for its transition to phase I. We observe a discontinuous transition around 7 K for c-axis fields between 1.3 and 1.8 T. Figure 8(a) depicts a color map representing the [100] thermal expansion coefficient of $EuAl_4$ taken on cooling at constant field. Lighter colors represent higher values of α_a. In this map we clearly observe the transition from the paramagnetic and field-polarized phase traced by the gray line. This continuous

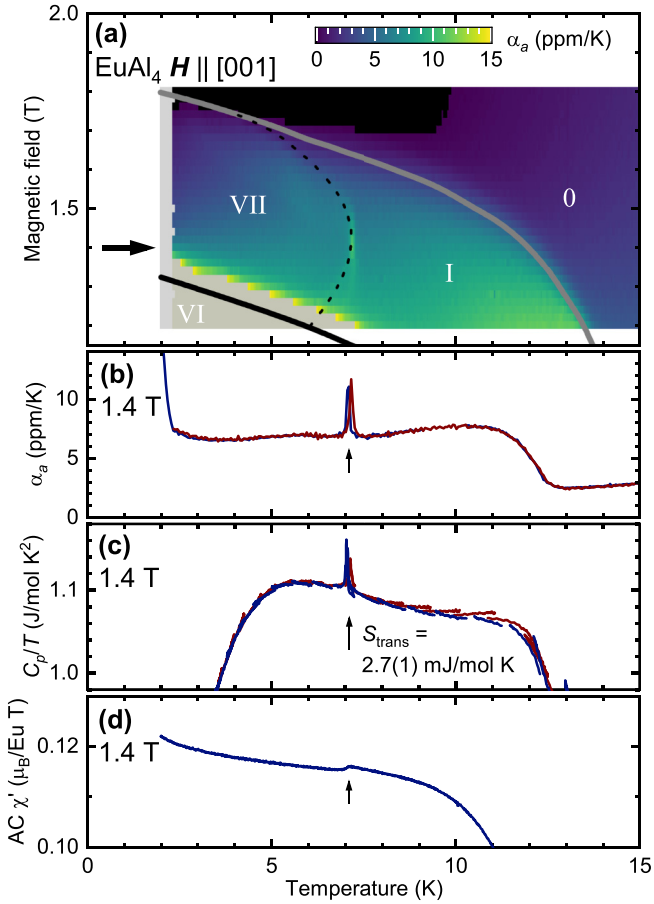

FIG. 8. Evidence for phase VII. (a) A color map representing the thermal expansion coefficient $\alpha_a(T, H)$, with the phase boundaries overlain. Data were taken on cooling and brighter colors represent larger CTE (black and gray are out of range). The dashed line traces peaks in $\alpha_a(T, H)$ we interpret as a transition between phases I and VII. The arrow on the left emphasizes the cut at 1.4 T presented in the lower panels. (b) The thermal expansion data taken on heating (red) and cooling (blue) at 1.4 T. (c) Heat-capacity data taken using the long-pulse method. Red and blue curves present data derived from the warming and cooling segments of each heat-pulse measurement. (d) AC magnetic susceptibility with a static DC field of 1.4 T taken on cooling displays a steplike feature at the I-VII transition.

transition manifests as a step in $\alpha_a(T, H)$ which appears in the color map as a relatively abrupt change in color.

The most important feature in this plot is the light colored, curving line highlighted by a black dotted line. This corresponds to a series of peaks in $\alpha_a(T)$ that evolve smoothly with field between 5 and 7 K. This feature separates phase fields I and VII, and is bounded at lower field by phase VI and merges with the saturation field near 1.75 T.

To investigate this transition, we will examine measurements taken at 1.4 T [noted by the arrow in Fig. 8(a)]. Figure 8(b) presents the thermal expansion curves taken on warming and cooling. At this field we observe two transitions: the continuous magnetic ordering transition near 12 K and the sharp peaks at 7.1 K (arrow). This peak corresponds to the I-VII phase boundary. It exhibits minor hysteresis (about 0.1 K) and a very tiny relative length change (order 0.6 ppm).

Both transitions also appear in the 1.4-T heat-capacity data [Fig. 8(c)]. Here again, we see discontinuous transition peaks in $C_p(T)/T$ near 7.1 K. We estimate the entropy of transformation to be 2.7(1) mJ/mol K. This is a minuscule 0.016% of the $R\ln(8) = 17.3$ J/mol K that the ordering of Eu^{2+} magnetic moments is expected to consume. This implies a rearrangement of the moments between two well-ordered magnetic phases.

Despite careful examination, we are unable to identify a signature of this I-VII phase transition in DC magnetization measurements. We do observe a subtle jump in the AC magnetic susceptibility. Figure 8(d) presents $\chi'(T)$ at 1.4 T taken on cooling. A small step is observed at 7.0 K corresponding to the peaks in α_a and heat capacity. This weak signature in $\chi'(T)$ implies a 0.6% change in the slope of $M(H)$. This transition clearly has only a small effect on the net magnetization of the material and explains why previous studies have not identified it.

The data presented in Fig. 8 reveal a subtle transition near 7 K that looks like a discontinuous phase transition. Next, we will describe why we believe this is a real transition. First, we observe this transition in three independent measurements on the same crystal and the transition temperatures are in excellent agreement. We do not believe the I-VII transition is related to an impurity phase or misaligned grains. Minor impurities are unlikely to produce features in heat capacity or dilatometry as these average over the entire sample volume. Finally, if the I-VII transition arose from an impurity phase or misaligned grain we would expect to see signatures extending beyond the previously observed transitions. Instead, we clearly see that the transition only appears in Fig. 8(a) for fields between the phase VI and the field-polarized phase (above 1.8 T).

We have now laid out our evidence for an additional magnetic phase in $EuAl_4$ and we will discuss the implications of phase VII in Sec. IV C.

E. Magnetic phase diagram

So far, we have presented the evidence for individual phase transitions based on our thermodynamic measurements. Now, we summarize the transitions identified in our data in Fig. 9. The × and + symbols represent transitions identified in temperature-dependent and field-dependent measurements, respectively. Error bars represent estimated transition widths. Solid lines trace the phase boundaries identified in the data.

There is exquisite agreement between the observed transitions extracted for the dilatometry, magnetization, and heat-capacity measurements in Figs. 9(a)–9(c). We also see that transitions identified in temperature-dependent (×) and field-dependent (+) data sets track the same phase boundaries. Critically, the first three measurements were done on the same crystal. This eliminates the challenge of comparing measurements on samples with different demagnetization factors (see Appendix B).

Resonant ultrasound spectroscopy (RUS) also shows evidence for the low-temperature magnetic transitions (see Appendix A). The critical fields we identified in field-dependent measurements are plotted in Fig. 9(d) and show agreement with the phase boundaries derived from the other

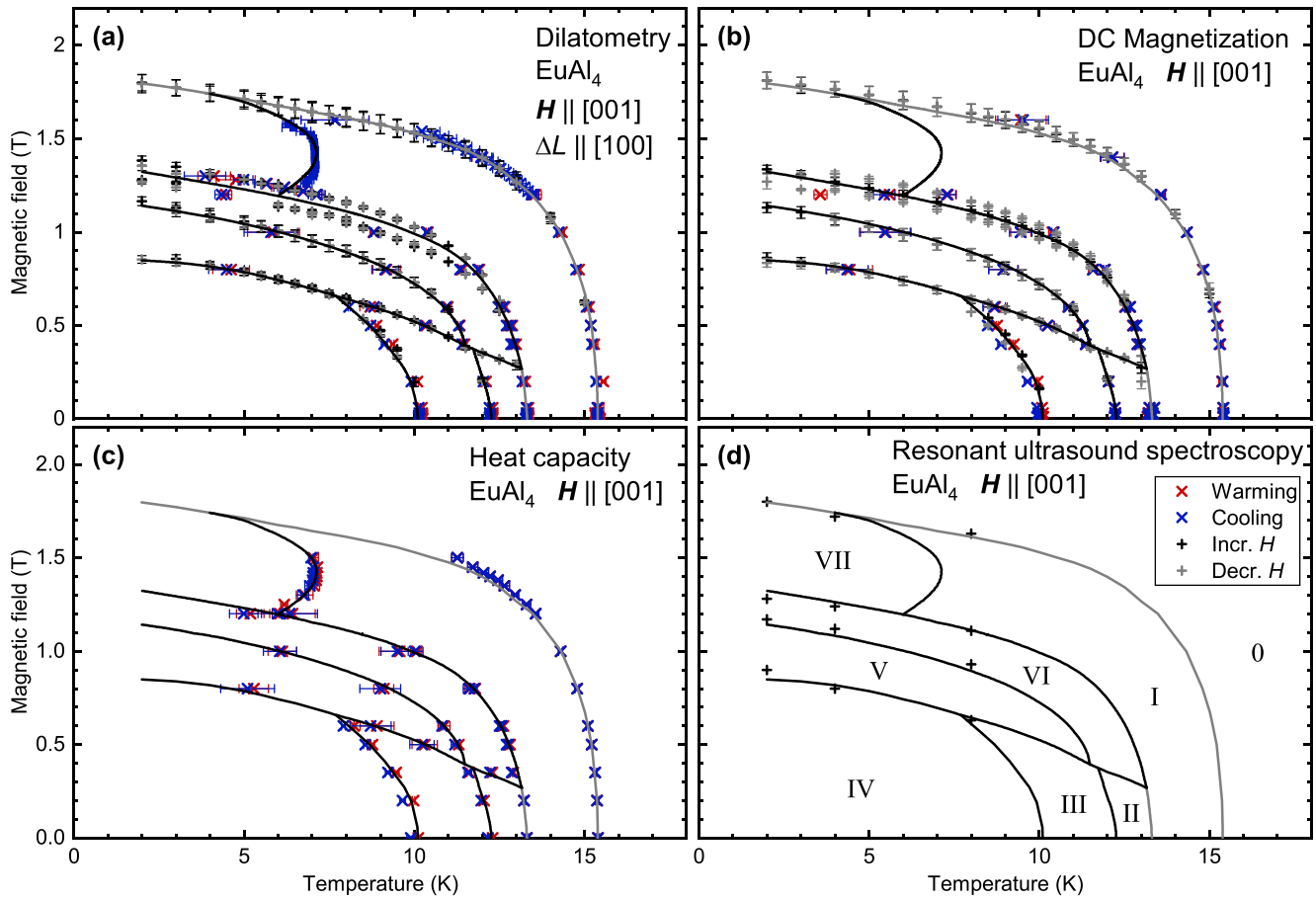

FIG. 9. Comparison of transitions observed in each measurement. Solid lines represent the phase boundaries we propose and the phases are labeled with roman numerals in (d). Black and gray lines represent transitions with discontinuous and continuous character. For every panel, × symbols indicate transitions observed in temperature-dependent measurements with red and blue representing warming and cooling, respectively. + signs indicate transitions identified in field-dependent measurements with black and gray symbols for increasing and decreasing field, respectively. Error bars represent estimated half-widths of the observed transitions. Magnetic field is the applied field, not corrected for demagnetization.

three measurements. All together, our thermodynamic results provide strong evidence for the phase diagram we propose.

IV. DISCUSSION

A. Distortions from tetragonal symmetry

In this section we will discuss which magnetic phases in the $\boldsymbol{H}$ ∥ [001] $EuAl_4$ phase diagram show strong deviations from tetragonal symmetry. Multi-Q topological spin textures can be enabled by tetragonal symmetries. Large lattice distortions break these symmetries and favor single-Q, nontopological orders. Therefore, it is important to examine which low-temperature magnetic phases in $EuAl_4$ exhibit strong symmetry-breaking strains. Phases III and IV have already been demonstrated to have lower symmetry [22] based on an $a \neq b$ distortion observed by x-ray diffraction (a B_{1g} mode). Our dilatometry results suggest that phase V exhibits the same distortion from tetragonal.

Figure 10 presents relative length changes of $EuAl_4$ along [100] as a function of field and temperature. Importantly, this measurement reveals breaking of $a = b$ tetragonal symmetry by a B_{1g} distortion [depicted as an inset in Fig. 10(b)].

Figure 10(a) presents the relative length change of the crystals on warming at constant field. First consider the lowest, zero-field curve. Note the large magnitude of the length change we observe at zero field. The sample changes in length by an impressive 1100 ppm (0.11%) between 2 and 20 K, suggesting a strong coupling of Eu magnetic order to the lattice. For comparison, we measured a 6.4-ppm thermal expansion of copper over the same temperature range.

Critically, the large length changes we observe in our dilatometry data provide a good estimate of the change in size of the unit cell and the magnitude of B_{1g} strain. Consider the gray ×'s in Fig. 10(a). These represent the relative change of the a lattice parameter determined by x-ray diffraction in Shimomura *et al.* [22] (shifted to match the dilatometry data at 16.5 K). The zero-field dilation data track the lattice parameter change closely, suggesting that crystal is nearly detwinned. This indicates that temperature dependence of $\Delta L/L$ presented in Fig. 10 is largely driven by change of $\Delta a/a$ brought about by B_{1g} distortion observed by Shimomura *et al.* in phases III and IV.

Examine the length changes in phases I and II above T_{N3}. These phases account for a modest part of the low-temperature length changes (50 and 37 ppm, respectively). This suggests

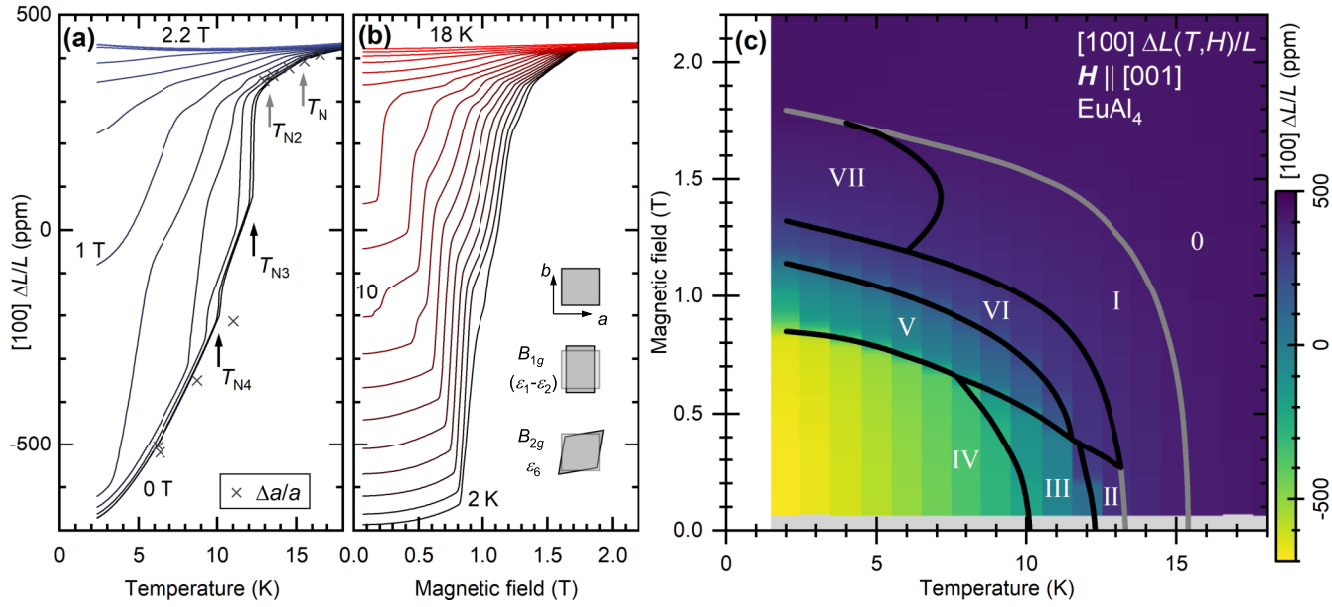

FIG. 10. Dilatometry results illustrating which phases show significant length changes. (a) The dilation vs temperature behavior taken on warming at fields from 0 to 2.2 T in 0.2-T steps. The sample is consistently longer at each higher applied field. Gray ×'s show the relative change in the a lattice parameter pulled from Shimomura *et al.* [22]. The close agreement with their results in our 0-T thermal expansion curve suggests that the sample is nearly detwinned (see Sec. IV A). (b) The dilation vs field behavior taken on increasing field with 1-K steps. The steplike and kinklike transitions evolve to lower fields at each higher temperature. The inset shows the in-plane distortion modes of a tetragonal system. Our [100] dilatometry measurement is sensitive to the B_{1g} mode. (c) Color map representing the relative length of the $EuAl_4$ crystal along [001] with the phase diagram superimposed. These measurements were taken at constant temperatures between 2 and 18 K with increasing field. Dark colors represent values closer to the paramagnetic phase 0 (i.e., 16 K, 0 T). Brighter colors represent H, T values where the crystal is significantly shorter.

that there is no significant B_{1g} distortion. It is important to note that our [100] dilatometry measurement is not sensitive to a B_{2g} in-plane shear distortion depicted in the inset of Fig. 10(b).

Shimomura *et al.* state that phases I and II appear to be tetragonal [22] because they did not observe peak splitting, indicating in-plane distortions. Despite this, a new diffraction report reveals that the CDW itself breaks tetragonal symmetry [21] at temperatures well above the magnetic transitions. Their data [21] are best modeled by an orthorhombic structure that would allow a B_{2g} strain. Critically, they also do not see a resolvable splitting of diffraction peaks, indicating that the distortion of the unit cell is limited. Therefore, phases I and II have only weakly broken tetragonal symmetry and might still be able to host multi-Q magnetic order.

Now that we have explored the zero-field thermal expansion results, we will examine the in-field behavior. The curves in Fig. 10(a) present the thermal expansion curves at fields from 0 to 2.2 T in 0.2-T steps. There are two primary observations: the sample length monotonically increases with field and we can see evolution of the step and kink phase transitions as a function of field. In other words, applying magnetic field and increasing temperature favors phases with smaller B_{1g} strains.

Figure 10(b) reveals both of the effects more clearly. This plot depicts sample deformation with increasing magnetic field at constant temperatures from 2 to 18 K in 1-K steps. Once again, we observe that the crystal lengthens along [100] as we increase both field and temperature. We can clearly observe many steplike and kinklike transitions evolving with temperature.

Our dilatometry results are summarized in Fig. 10(c) highlighting which phases show a strong distortion from tetragonal symmetry (lighter colors). This plot presents the relative length change of the $EuAl_4$ crystal along [100] as a function of temperature and applied field along the c axis. Colors represent the value of $\Delta L/L$. Darker shades represent T, H values where the sample is longer and close to its length in the paramagnetic phase 0 above T_N. Lighter colors represent regions where the crystal is significantly shorter.

In Fig. 10(c), phases III, IV, and V have lighter colors representing a large contraction from the paramagnetic phase 0. This implies that these three phases possess a strong B_{1g} distortion. In contrast, the sample length in phases I, II, VI, and VII are quite close to the length of phase 0, represented by dark colors. This indicates that these phases likely have $a = b$.

We should note that there are clear differences in the magnetism of the low-temperature field-polarized regime and the paramagnetic (dynamic, disordered) regime that are both generically labeled as phase 0. However, our results suggest this has a limited impact on the [100] dilation of the material, especially in comparison to the effect that the ground-state magnetic orderings have on the dilation.

This leads us to the implications of our dilatometry results for skyrmions and merons in $EuAl_4$. The strong B_{1g}

distortion we observe in phases III, IV, and V make them unlikely hosts for the multi-Q topological magnetic textures. Our dilatometry results reveal only weak length changes along [100] in phases I, II, VI, and VII, suggesting that they have nearly equal a and b lattice parameters. It is unlikely that these phases have full tetragonal symmetry because of the orthorhombic CDW modulation [21]. Despite this, previous diffraction reports [21,22] and our dilatometry results suggest that there may only be weak breaking of tetragonal symmetries. Therefore, phases I, II, VI, and VII might host multi-Q phases such as skyrmion or meron crystals.

B. Characteristics of phases and transitions

1. Phases I and II

First we will take a closer look at phases I and II and the transition between them. Kaneko *et al.* [25] report magnetic propagation vectors of $\boldsymbol{Q} = (q, q, 0)$ and $(q, -q, 0)$ r.l.u. in both phases (see Fig. 1). The magnetic periodicities within these phases are nearly equal with $q = 0.086(4)$ and 0.085(4) r.l.u. at 13.5 and 12.5 K, respectively. We suspect these phases are almost tetragonal and share nearly equal $\boldsymbol{Q}$'s. What differentiates these phases?

Our magnetic measurements reveal that phases I and II have different low-field magnetic behavior. The transition between them appears discontinuous in dilatometry, heat capacity, and AC susceptibility, but only for small applied field. For fields larger than 5 mT the transition appears continuous.

This might be due to weak ferromagnetism in phase II. Low-field (0.01 T) DC magnetization measurement and AC susceptibility data show different behavior [Figs. 5(d) and 5(e), respectively]. The DC $M(T)$ displays a elevated value within phase II in contrast to the flatter value of AC $\chi'(T)$ in the same temperature range. $\chi''(T)$ shows an 80% higher value in phase II, indicating that there is lossy mechanism within the phase. Together, these magnetic data suggest that phase II has a small ferromagnetic contribution.

2. Phases III and IV

In this section, we will discuss the characteristics of the two low-temperature and low-field phases, III and IV. These phases both clearly break tetragonal symmetry with $a \neq b$ [22] reflected in our dilatometry results (see Sec. IV A). Also, these phases share similarities in their magnetic order. Neutron diffraction reveals that phases III and IV host incommensurate antiferromagnetism with wave vectors $(q, 0, 0)$ or $(0, q, 0)$ [25]. These similarities between phases III and IV raise two questions: What distinguishes these two phases and why are they separated by a discontinuous, hysteretic transition at T_{N4}?

The III-IV transition at T_{N4} might herald the appearance of an additional component of the $(q, 0, 0)$ modulated magnetism. It is curious that this would happen abruptly at a hysteretic, discontinuous transition. Alternatively, the transition might represent a discontinuity in $q(T)$. To this point, distinctly different magnetic wave vectors are observed at 11.5 and 4.3 K with $q = 0.17(1)$ and 0.194(5) r.l.u., respectively [25].

Maybe the transition is driven to be discontinuous by competition between the $(q, 0, 0)$ magnetism and the charge-density-wave degree of freedom. X-ray diffraction results reveal that the lattice has a strong response on cooling into phase III [22]. The intensity of the CDW satellite peaks drops by 21% across T_{N3} and the intensity of the (600) peak falls by 33%. The magnetic transitions at T_N and T_{N2} do not demonstrate such strong coupling to the lattice. The transition between phases III and IV might be a consequence of the competition between the magnetic and lattice modulations.

3. II-VI and III-V transitions

In Sec. III C we presented the evidence for phase transitions between phases II and VI as well phases III and V. Previous studies did not observe these transitions [18,24]. This is likely because they used wider temperature and field steps. In this section we will discuss the nature of these transitions and their implications.

The transition between phases II and VI is clear in both field-dependent and temperature-dependent measurements. These phases show only minor differences in magnetic response [Fig. 7(d)] but different magnetostriction coefficients [Fig. 7(h)]. These changes in magnetic and dilation behavior suggest a relatively subtle reconfiguration of the magnetic order.

In contrast, the III-V transition shows significant changes in the thermodynamic properties of $EuAl_4$. First, consider the dramatic change in magnetization at this transition (10.3 K) observed in Fig. 6(d). This shows that phase V has a significantly higher magnetization than phase III. This is directly reflected in the $M(\mu_0 H)$ plots in Figs. 7(b) and 7(c) as sharp jumps in the magnetization at 0.59 and 0.48 T, respectively. The dilatometry also reveals significant sample expansion across this transition in Figs. 7(f) and 7(g). Both $M(\mu_0 H)$ and $\Delta L(\mu_0 H)/L$ are notably nonlinear in phase V with rising slopes with increasing field.

The transition between phases III and V represents a more dramatic change in the magnetic order than the II-VI transition. For example, the jump in $M(\mu_0 H)$ might reflect a change from cycloidal or helical order in phase III to a fan or conical phase V. This could also explain the nonlinear field dependence of properties of phase V in Figs. 7(b), 7(c), 7(f), and 7(g).

The II-VI and III-V transitions we report are clear additions to the $\boldsymbol{H} \parallel [001]$ $EuAl_4$ phase diagram. A detailed examination of the magnetic order by single-crystal diffraction under field will provide insights into the intricate competition between the magnetic and lattice subsystems at play $EuAl_4$.

4. I-VI transition

The I-VI phase boundary has unique character in this system. The transition consistently appears as a split feature in magnetic, heat-capacity, and dilatometric measurements. This double feature is clearly visible in Figs. 7(b), 7(c), 7(f), and 7(g) (1.05 T at 9 K and 0.95 T at 10.5 K). The thin $\frac{dM}{d(\mu_0 H)}$ plots show a shoulder-peak feature and the $\lambda_a(\mu_0 H)$ shows a double-peak feature separated by roughly 0.06 T.

In Fig. 9 we attempt to capture this split transition by plotting the estimated centers of peaks in $C_p(T)$ and the

derivatives of $\Delta L/L$ and M. These points form two lines on either side of the boundary between I and VI phase fields. Note that the split features track the same trends for both field- and temperature-dependent measurements.

The split I-VI phase transition might represent an unusual manifestation of a transition broadened by demagnetization effects (Appendix B) or there might be an additional phase in-between these peaks. We suggest that future experiments devote some attention to the regions between phases I and VI and between VI and VII to uncover further clues about this unusual transition.

C. What do we know about phase VII?

Finally, we will examine the nature of our most interesting phase in $EuAl_4$, phase VII. We propose that this distinct phase appears below 7 K between 1.2 and 1.8 T based on our measurements presented in Sec. III D. Figure 8 reveals a discontinuous transition bounding this region based on dilatometry, heat-capacity, and AC magnetic susceptibility measurements.

Phase VII has special importance in this system as Shang *et al.* revealed that this H, T region may host a topological Hall effect [24]. As the authors discuss, this signal does not appear to arise from an anomalous Hall contribution due to the uniform magnetization. Instead, a noncollinear magnetic texture is anticipated to explain this topological Hall response.

Although skyrmions are implicated in Ref. [24], other topological magnetic phases could generate the observed Hall contribution in this region [14]. For example, some meron crystals and domain structures host a net vector spin chirality which generates the topological Hall contribution.

Does $EuAl_4$ host a skyrmion or meron crystal in phase VII? In short, maybe. These magnetic orders could explain the pocketlike phase field. First, all the meron and skyrmion crystals are consistently bounded by discontinuous phase transition [11,13,14]. This appears to be the case for phase VII [see Fig. 8(a)].

Second, the skyrmion crystal and one of the meron crystals in Wang *et al.* that have a finite vector spin chirality (SkX and MX-I) appear for finite applied field and have net magnetization [14]. In fact, for the parameters they explore, the skyrmion crystal phase is generally adjacent to or near the field-polarized phase 0. This is exactly the case for phase VII in $EuAl_4$; it appears at low temperature just below the saturation field with nearly saturated magnetization. This observation is suggestive of a skyrmion crystal in phase VII.

Next, we return to broken tetragonal symmetry in the magnetic phases of $EuAl_4$. The multi-Q meron crystals and a square skyrmion should be hosted by tetragonal materials. Domains of the 3-Q triangular skyrmion crystal discussed in Ref. [14] might only lead to weak strains of a bulk sample. Our results suggest that both phases I and VII are nearly tetragonal based on our dilatometry measurements but the coexisting CDW modulation appears to break fourfold symmetry [21]. This situation would favor single-Q magnetic orders. It is possible that a weakly modified tetragonal phase could host the multi-Q magnetic textures and produce a topological Hall signal in phase VII.

An argument against skyrmions in phase VII is the $M(\mu_0 H)$ behavior we observe (see Fig. 13). Like others before, we observe a simple change in slope at the saturation field [18,24]. In many experimental reports [11,13] and theoretical predictions [5,6,8], skyrmion crystals generate a terracelike feature in $M(\mu_0 H)$ with reduced slope. Our $\chi'(T)$ data show a very weak reduction in dM/dH on cooling into phase VII but no clear terrace region is obvious in $M(\mu_0 H)$ curves. In addition, we would not expect a skyrmion or meron crystal to exist with a nearly saturated magnetization.

D. Outlook

Here we will examine experimental tests for skyrmion and meron phases in $EuAl_4$. Phase VII should be checked for these topological magnetic textures. Three techniques are commonly employed to identify these magnetic configurations and differentiate them from their mundane, single-Q counterparts. Real-spacing imagining of skyrmions is often performed using Lorentz transmission electron microscopy. Unfortunately, phase VII appears below 7 K, a challenging temperature regime for sample stages. Single-crystal neutron or resonant x-ray diffraction under a [001] magnetic field are both clear options. We would expect to observe harmonics of the magnetic wave vectors in the case of mulit-Q order [e.g., intensity at $(2q, 0, 0)$ for $(q, q, 0) + (q, -q, 0)$ order]. Neutron diffraction, although clearly possible [25], is challenged by Eu's strong neutron absorption. This makes resonant x-ray scattering a strong choice.

To summarize, skyrmion or meron magnetic textures are good candidates for producing the Hall signal observed $EuAl_4$ within phase VII. The characteristics of this phase and its location in the phase diagram are reminiscent of a skrmion or meron crystal. We propose an in-field resonant x-ray diffraction experiment to examine phase VII for evidence of these topological magnetic textures. In addition, we believe that a diffraction study of the other $\boldsymbol{H} \parallel [001]$ magnetic phases will help uncover the competing interactions that drive the complex magnetism in $EuAl_4$.

V. CONCLUSIONS

$EuAl_4$ shows a rich variety of low-temperature orders. It hosts both lattice modulations and complex magnetic phases. We explored the $\boldsymbol{H} \parallel [001]$ phase diagram in great detail using a series of thermodynamic measurements. Dilatometry, heat capacity, DC magnetization, AC magnetic susceptibility, and resonant ultrasound spectroscopy revealed not only the numerous transitions, but also clues about their nature.

We observed all the previously reported low-temperature transitions including T_{CDW} and magnetic transitions. We also reported three phase transitions giving a total of seven magnetic phases under a c-axis magnetic field. The resulting detailed magnetic phase diagram (Fig. 2) is the first important outcome from this study and will guide future investigations of the numerous magnetic phases of $EuAl_4$.

We discussed the characteristics of these phases and suggest that the distinction between phases be examined in detail. In particular, the I-II and III-IV transitions have curious features and warrant further study. It is not clear what differentiates the similar phases.

Finally, we presented evidence of a consequential phase, phase VII. Its phase field directly coincidences with the region where a skyrmion phase was proposed based on an enhanced anomalous Hall signal. Our measurements suggest that this phase has some characteristics that can be caused by magnetic topological textures. We advocate for a detailed diffraction study to examine this potential skyrmion phase and look for distortions from tetragonal symmetry. In addition, determining the order parameters that describe the other phases in the system will offer insights into the competing interactions which underlie the intricate magnetic phase diagram of $EuAl_4$ that we delineated in this study.

Note added in proof. Recently, results reported by Takagi *et al.* suggest that skyrmions are present in $EuAl_4$ in phases V and VI, not phase VII [41]. The results in this paper suggest that the average symmetry of the crystal lattice is rather different in phases V and VI. In total, all of the recent works on EuAl4 reveal that there is still much to be understood about this complex material.

ACKNOWLEDGMENTS

We would like to thank C. Batista, S. Gao, S. Do, and A. Christianson for their helpful discussions about topological magnetic textures. We would like to thank B. Chakoumakos for his low-temperature single-crystal XRD measurements. M.Y. Hu and E. E. Alp (Argonne) are acknowledged for assistance for NRIXS data acquisition at 3-ID. Research was supported by the U.S. Department of Energy, Office of Science, Basic Energy Sciences, Materials Sciences and Engineering Division (under Contract No. DE-AC05-00OR22725). J.R.T. was supported by ORNL Laboratory Directed Research and Development (LDRD) funds. W.R.M. acknowledges partial support for writing from the Gordon and Betty Moore Foundation's EPiQS Initiative, Grant No. GBMF9069. This research used resources of the Advanced Photon Source, a U.S. Department of Energy (DOE) Office of Science User Facility operated for the DOE Office of Science by Argonne National Laboratory under Contract No. DE-AC02-06CH11357.

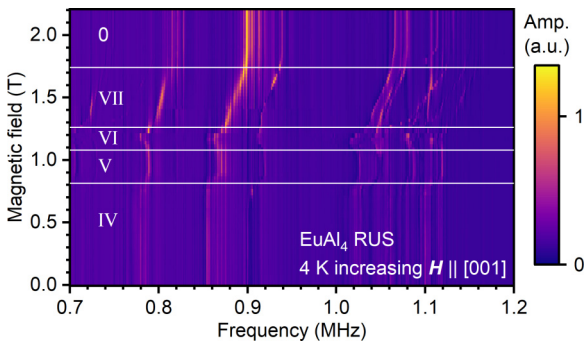

FIG. 11. Resonant ultrasound spectroscopy from the $EuAl_4$ sample under increasing c-axis magnetic field. Bright colors represent stronger mechanical resonant response of the sample near resonant modes. Each row represents a spectrum taken while ramping field. The horizontal lines shows the critical fields of the metamagnetic transitions based on the other measurements in this paper.

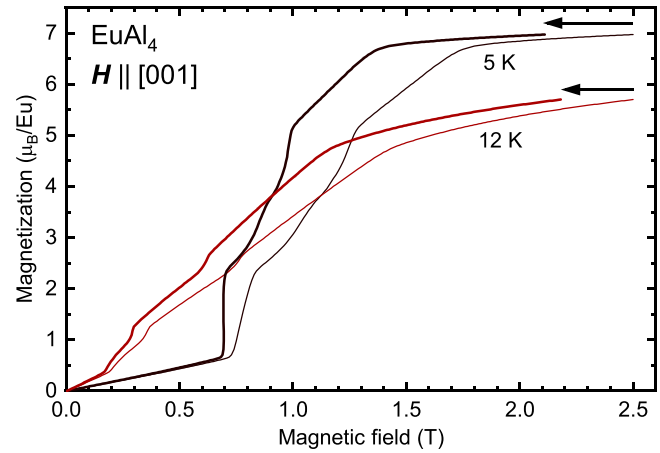

FIG. 12. Magnetization vs field plots for $EuAl_4$ illustrating demagnetization corrections. The thin lines represent measured $M(\mu_0 H)$ plots. The thicker plots present $M(\mu_0 H_{\text{internal}})$ based on an estimated demagnetization correction to the applied field. Arrows illustrate the mapping of $H_{\text{applied}} \rightarrow H_{\text{internal}}$.

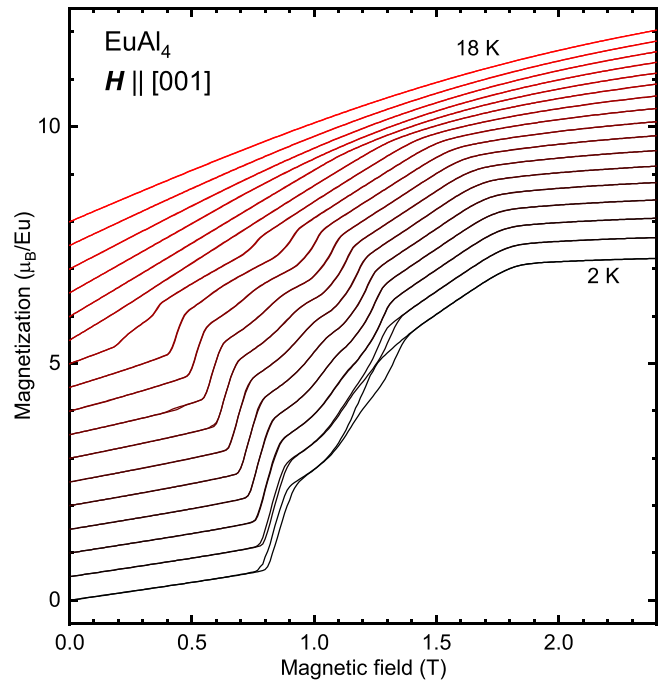

FIG. 13. $M(\mu_0 H)$ plots for $EuAl_4$ with field along the c axis. Each curve presents the magnetization between 2 and 18 K in 1-K steps offset by 0.5 μB/Eu. Data obtained while increasing and decreasing field are presented for each temperature and hysteresis is evident at transitions in the 2- and 3-K plots.

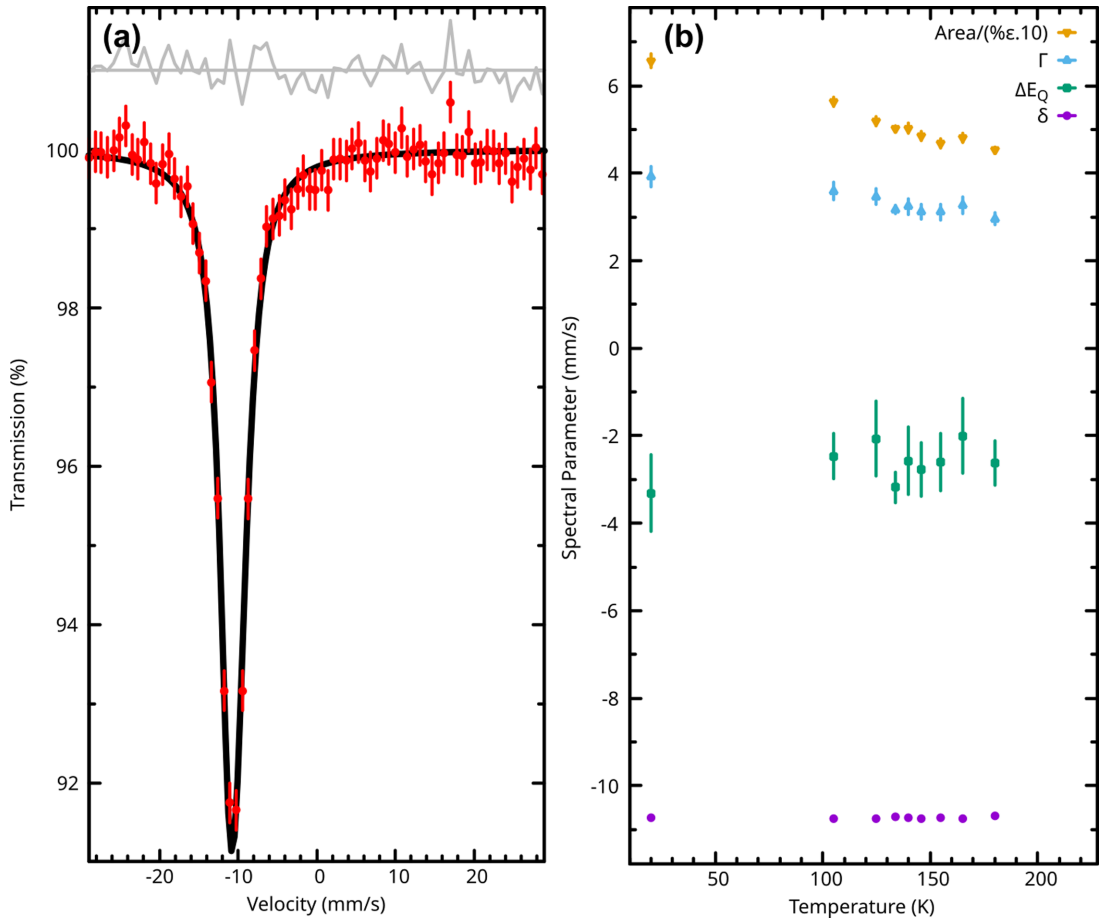

FIG. 14. Temperature-dependent ^{151}Eu Mössbauer results. (a) ^{151}Eu Mössbauer spectrum of $EuAl_4$ at 146 K; data in red, fit in black, and residuals in gray. (b) Spectral parameters as function of temperature. Γ, ΔE_Q, and δ are the linewidth (FWHM), quadrupole splitting, and isomer shift, respectively. The spectral area is in % effect mm/s (scaled by a factor 10).

results of federally sponsored research in accordance with the DOE Public Access Plan [42].

APPENDIX A: RESONANT ULTRASOUND SPECTROSCOPY

Low-temperature, field-dependent resonant ultrasound spectroscopy (RUS) shows clear signals of the magnetic transitions in $EuAl_4$. Figure 11 presents resonant ultrasound spectra of a $EuAl_4$ sample on increasing field at 4 K. Bright colors represent stronger mechanical response corresponding to resonant modes. Just as we discussed in Sec. III A, shifts in the frequencies of resonant modes reflect changes in the elastic moduli. The four metamagnetic transitions (horizontal white lines) correspond to jumps in the peak positions or changes in the rate of frequency change vs field. On the whole, resonant modes shift to higher frequencies at higher field, reflecting a stiffening of the lattice. Low-temperature resonant ultrasound spectroscopy (RUS) measurements were challenging to interpret and temperature-dependent measurements suffered very large temperature errors.

APPENDIX B: DEMAGNETIZATION EFFECTS

A magnetized sample produces an inhomogeneous internal field referred to as the demagnetization field. As a result, the local field varies throughout sample with values below that of the applied field. Throughout this study we do not correct for the demagnetization field (but it can be done; Ref. [10]). Careful understanding of sample geometry is critical but the correction can be accomplished for spheres, rectangular prisms, and ellipsoids [43].

The key impact of the demagnetization correction is a remapping of all field-dependent data to lower field values based on the magnetization and sharpening discontinuous transitions. The expression in SI is

$$H_{\text{internal}} = H_{\text{applied}} - NM, \tag{B1}$$

where N is the demagnetization factor [43]. M and H values need to be in A/m. Examples of this remapping are presented for 5- and 12-K $M(\mu_0 H)$ plots in Fig. 12 with a demagnetization factor of $N = 0.52$. This value was chosen because it gives vertical $M(\mu_0 H)$ at the discontinuous transitions [44]. Notably, it agrees well with the magnetometric demagnetization factor of $N = 0.48$, which we estimate from the tables in Ref. [43] using our sample dimensions (Sec. II C).

The mapping illustrated in Fig. 12 reduces fields by up to 20% due to the significant magnetization from the large europium moments. These likely explain the differences in reported fields for the metamagnetic phase transitions in Refs. [18,24]. For example, these report saturation fields for

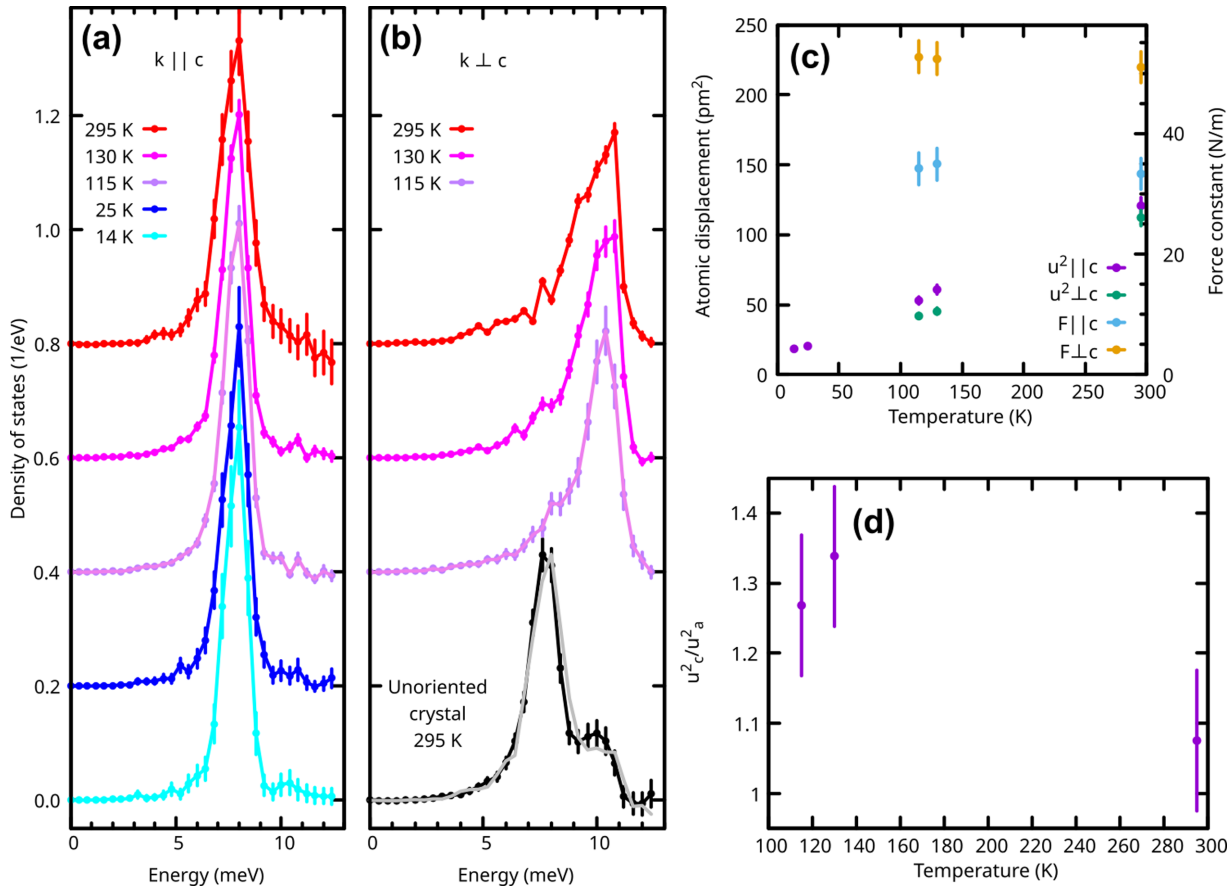

FIG. 15. Temperature-dependent ^{151}Eu nuclear resonant inelastic x-ray scattering (NRIXS) results. (a), (b) Density of europium vibrational states parallel and perpendicular to c at the indicated temperatures. The unoriented crystal data at ambient conditions can be modeled by linear combination (in gray) of data at 295 K parallel (78%) and perpendicular (22%) to c. (c) Temperature dependence of the Eu force constant F and dynamic atomic displacement parameter u^2 parallel and perpendicular to c. (d) The anisotropy in u^2. A 5% error bar on u^2 and F is estimated.

$\boldsymbol{H} \parallel [001]$ of 1.5 and 2.0 T, respectively. After demagnetization correction, we estimate a saturation field of 1.4 T at 2 K.

Stryjewski and Giordano (Ref. [44]) note that demagnetization effects have important implications for experimental appearance of discontinuous metamagnetic transitions. The demagnetization field leads to coexistence of the low- and high-field phases over a range of applied fields leading to a broadened transition. In addition, phase coexistence could limit and obscure any hysteresis across the discontinuous transition. Without demagnetization field (like in a needlelike sample) we would expect discontinuous $M(\mu_0 H)$ curves at discontinuous metamagnetic transitions.

The slope of $\frac{dM}{dH} \propto 1/N$, where H is the applied field and N is the demagnetization factor [44]. This means that transitions with larger changes in magnetization ΔM will exhibit wider transitions due to demagnetization effects: $\Delta H \propto N\,\Delta M$.

This effect is pronounced at this III-V transition because it has a large ΔM and a shallow slope in the phase diagram. Like many of the discontinuous transitions in this system, the III-V transition did not show hysteresis with field- or temperature-dependent measurements but shows a broad transition width. The transition is broader than others we observe, especially in temperature-dependent measurements (Fig. 6 near 10.3 K).

The shallow slope of III-V phase boundary line also explains why the transition appears unusually broad in the temperature-dependent measurements in Fig. 6. We estimate full width at half-maximum of the transition to be 0.8 K in Fig. 6 and 0.05 T in the 10.5-K field-dependent measurements [Figs. 7(c) and 7(g)]. The ratio of these values is 0.06 T/K very close to the absolute value of the slope of the III-V phase boundary line, 0.08 T/K. This means that the anomalously broad transition in Fig. 6 is explained by the slope of transition line and demagnetization effects. Although not shown here, the transition between phases IV and V is also notably broad and has a large ΔM.

APPENDIX C: MAGNETIZATION VS FIELD

Figure 13 presents the magnetization vs magnetic field data between 2 and 18 K. The metamagnetic transitions discussed throughout the paper are evident as kinks and jumps in the plots. Observe how the transitions shift to lower temperatures as temperature increases. Plots for both increasing and decreasing field are displayed at each temperature but hysteresis is only observed for low-temperature curves and at the III-IV transition near 0.43 T at 9 K.

APPENDIX D: MÖSSBAUER AND NRIXS

Mössbauer spectra feature a single absorption line depicted in Fig. 14(a). The temperature dependence of the fit parameters appear in Fig. 14(b). Detailed analysis reveals broadening by a small quadrupole splitting, which consistently is about −3 mm/s and an isomer shift of −10.8 mm/s. The isomer shift is consistent with an earlier report [45], and close to a report [23] where the reference used for the isomer shift was not specified. Upon cooling, the linewidth is increasing due to thickness broadening.

The Eu-specific nuclear inelastic scattering for $EuAl_4$ was obtained at 115, 130, and 295 K with the beam parallel and perpendicular to c. In addition, data were obtained at 13.5 and 25 K with the beam parallel to c and one spectrum at 295 K on an unoriented crystal. The corresponding directionally projected density of Eu vibrational states, $g(E)$, is presented in Figs. 15(a) and 15(b). These were obtained by the usual log-Fourier procedure [46] using the NISDOS code, a modified version of the program DOS [47,48]. Anisotropic vibrations for Eu are evidenced by the shape of $g(E)$ which is dominated by a single peak at 8 and 10.5 meV for the c and a projected data, respectively.

From weighted integrals of the density of vibrational states, we have extracted the atomic displacement parameters and force constants [Fig. 15(c)] using the same procedure as in Ref. [49]. We do not observe any qualitative change in $g(E)$ as a function of temperature, indicating that any change to Eu phonons across the CDW transition is small or limited to a narrow region of reciprocal space. The temperature dependence of the force constant F reveals the typical softening with increasing temperature. The temperature dependence of the dynamic atomic displacement parameter along c and a indicates the typical increase as function of temperature. Closer inspection reveals that dynamic atomic displacements are mostly isotropic at 295 K and have 30% anisotropy below the CDW transition ($u_c^2 \approx 1.3\ u_a^2$) as depicted in Fig. 15(d).

[1] Y. Tokura and N. Kanazawa, Magnetic skyrmion materials, Chem. Rev. **121**, 2857 (2020).

[2] B. Göbel, I. Mertig, and O. A. Tretiakov, Beyond skyrmions: Review and perspectives of alternative magnetic quasiparticles, Phys. Rep. **895**, 1 (2021).

[3] C. Back, V. Cros, H. Ebert, K. Everschor-Sitte, A. Fert, M. Garst, T. Ma, S. Mankovsky, T. L. Monchesky, M. Mostovoy, N. Nagaosa, S. S. P. Parkin, C. Pfleiderer, N. Reyren, A. Rosch, Y. Taguchi, Y. Tokura, K. von Bergmann, and J. Zang, The 2020 skyrmionics roadmap, J. Phys. D: Appl. Phys. **53**, 363001 (2020).

[4] S.-Z. Lin and S. Hayami, Ginzburg-Landau theory for skyrmions in inversion-symmetric magnets with competing interactions, Phys. Rev. B **93**, 064430 (2016).

[5] A. O. Leonov and M. Mostovoy, Multiply periodic states and isolated skyrmions in an anisotropic frustrated magnet, Nat. Commun. **6**, 8275 (2015).

[6] S. Hayami, S.-Z. Lin, and C. D. Batista, Bubble and skyrmion crystals in frustrated magnets with easy-axis anisotropy, Phys. Rev. B **93**, 184413 (2016).

[7] T. Okubo, S. Chung, and H. Kawamura, Multiple-q States and the Skyrmion Lattice of the Triangular-Lattice Heisenberg Antiferromagnet Under Magnetic Fields, Phys. Rev. Lett. **108**, 017206 (2012).

[8] R. Yambe and S. Hayami, Skyrmion crystals in centrosymmetric itinerant magnets without horizontal mirror plane, Sci. Rep. **11**, 11184 (2021).

[9] Z. Wang, Y. Su, S.-Z. Lin, and C. D. Batista, Skyrmion Crystal from RKKY Interaction Mediated by 2D Electron Gas, Phys. Rev. Lett. **124**, 207201 (2020).

[10] M. Hirschberger, T. Nakajima, S. Gao, L. Peng, A. Kikkawa, T. Kurumaji, M. Kriener, Y. Yamasaki, H. Sagayama, H. Nakao, K. Ohishi, K. Kakurai, Y. Taguchi, X. Yu, T. hisa Arima, and Y. Tokura, Skyrmion phase and competing magnetic orders on a breathing kagomé lattice, Nat. Commun. **10**, 5831 (2019).

[11] N. D. Khanh, T. Nakajima, X. Yu, S. Gao, K. Shibata, M. Hirschberger, Y. Yamasaki, H. Sagayama, H. Nakao, L. Peng, K. Nakajima, R. Takagi, T. hisa Arima, Y. Tokura, and S. Seki, Nanometric square skyrmion lattice in a centrosymmetric tetragonal magnet, Nat. Nanotechnol. **15**, 444 (2020).

[12] T. Kurumaji, T. Nakajima, M. Hirschberger, A. Kikkawa, Y. Yamasaki, H. Sagayama, H. Nakao, Y. Taguchi, T. hisa Arima, and Y. Tokura, Skyrmion lattice with a giant topological Hall effect in a frustrated triangular-lattice magnet, Science **365**, 914 (2019).

[13] S. Spachmann, A. Elghandour, M. Frontzek, W. Löser, and R. Klingeler, Magnetoelastic coupling and phases in the skyrmion lattice magnet Gd_2 $PdSi_3$ discovered by high-resolution dilatometry, Phys. Rev. B **103**, 184424 (2021).

[14] Z. Wang, Y. Su, S.-Z. Lin, and C. D. Batista, Meron, skyrmion, and vortex crystals in centrosymmetric tetragonal magnets, Phys. Rev. B **103**, 104408 (2021).

[15] K. Mitsumoto and H. Kawamura, Skyrmion crystal in the RKKY system on the two-dimensional triangular lattice, Phys. Rev. B **105**, 094427 (2022).

[16] K. Momma and F. Izumi, VESTA3 for three-dimensional visualization of crystal, volumetric and morphology data, J. Appl. Crystallogr. **44**, 1272 (2011).

[17] A. Nakamura, Y. Hiranaka, M. Hedo, T. Nakama, Y. Miura, H. Tsutsumi, A. Mori, K. Ishida, K. Mitamura, Y. Hirose, K. Sugiyama, F. Honda, T. Takeuchi, T. D. Matsuda, E. Yamamoto, Y. Haga, and Y. Ōnuki, Unique Fermi surface and emergence of charge density wave in $EuGa_4$ and $EuAl_4$, in *Proceedings of the International Conference on Strongly Correlated Electron Systems (SCES2013)* (The Physical Society of Japan, Tokyo, 2014), p. 011012.

[18] A. Nakamura, T. Uejo, F. Honda, T. Takeuchi, H. Harima, E. Yamamoto, Y. Haga, K. Matsubayashi, Y. Uwatoko, M. Hedo, T. Nakama, and Y. Ōnuki, Transport and magnetic properties of $EuAl_4$ and $EuGa_4$, J. Phys. Soc. Jpn. **84**, 124711 (2015).

[19] A. Nakamura, T. Uejo, H. Harima, S. Araki, T. C. Kobayashi, M. Nakashima, Y. Amako, M. Hedo, T. Nakama, and Y. Ōnuki, Characteristic Fermi surfaces and charge density wave in $SrAl_4$

and related compounds with the $BaAl_4$-type tetragonal structure, J. Alloys Compd. **654**, 290 (2016).

[20] S. Araki, Y. Ikeda, T. C. Kobayashi, A. Nakamura, Y. Hiranaka, M. Hedo, T. Nakama, and Y. Ōnuki, Charge density wave transition in $EuAl_4$, J. Phys. Soc. Jpn. **83**, 015001 (2014).

[21] S. Ramakrishnan, S. R. Kotla, T. Rekis, J.-K. Bao, C. Eisele, L. Noohinejad, M. Tolkiehn, C. Paulmann, B. Singh, R. Verma, B. Bag, R. Kulkarni, A. Thamizhavel, B. Singh, S. Ramakrishnan, and S. van Smaalen, Orthorhombic charge density wave on the tetragonal lattice of $EuAl_4$, IUCrJ, **9**, 378 (2022).

[22] S. Shimomura, H. Murao, S. Tsutsui, H. Nakao, A. Nakamura, M. Hedo, T. Nakama, and Y. Ōnuki, Lattice modulation and structural phase transition in the antiferromagnet $EuAl_4$, J. Phys. Soc. Jpn. **88**, 014602 (2019).

[23] H. H. Wickman, I. Nowik, J. H. Wernick, D. A. Shirley, and R. B. Frankel, Hyperfine fields and isomer shifts in magnetically ordered europium compounds, J. Appl. Phys. **37**, 1246 (1966).

[24] T. Shang, Y. Xu, D. J. Gawryluk, J. Z. Ma, T. Shiroka, M. Shi, and E. Pomjakushina, Anomalous Hall resistivity and possible topological Hall effect in the $EuAl_4$ antiferromagnet, Phys. Rev. B **103**, L020405 (2021).

[25] K. Kaneko, T. Kawasaki, A. Nakamura, K. Munakata, A. Nakao, T. Hanashima, R. Kiyanagi, T. Ohhara, M. Hedo, T. Nakama, and Y. Ōnuki, Charge-density-wave order and multiple magnetic transitions in divalent europium compound $EuAl_4$, J. Phys. Soc. Jpn. **90**, 064704 (2021).

[26] H. Zhang, X. Y. Zhu, Y. Xu, D. J. Gawryluk, W. Xie, S. L. Ju, M. Shi, T. Shiroka, Q. F. Zhan, E. Pomjakushina, and T. Shang, Giant magnetoresistance and topological Hall effect in the $EuGa_4$ antiferromagnet, J. Phys.: Condens. Matter **34**, 034005 (2021).

[27] J. M. Moya, S. Lei, E. M. Clements, K. Allen, S. Chi, S. Sun, Q. Li, Y. Y. Peng, A. Husain, M. Mitrano, M. J. Krogstad, R. Osborn, P. Abbamonte, A. B. Puthirath, J. W. Lynn, and E. Morosan, Incommensurate magnetic orders and possible field-induced skyrmions in the square-net centrosymmetric $EuGa_2Al_2$ system, arXiv:2110.11935.

[28] P. H. Tobash and S. Bobev, Synthesis, flux crystal growth, structure and properties of the new rare-earth compounds $EuAl_{4-x}Si_x$ ($x \sim 1$), TmAlSi and LuAlSi, J. Alloys Compd. **418**, 58 (2006).

[29] M. Stavinoha, J. A. Cooley, S. G. Minasian, T. M. McQueen, S. M. Kauzlarich, C.-L. Huang, and E. Morosan, Charge density wave behavior and order-disorder in the antiferromagnetic metallic series $Eu(Ga_{1-x}Al_x)_4$, Phys. Rev. B **97**, 195146 (2018).

[30] M. L. Stavinoha, Magnetic and electronic correlations in rare earth intermetallic compounds, Ph.D. thesis, Rice University, 2019.

[31] P. C. Canfield, T. Kong, U. S. Kaluarachchi, and N. H. Jo, Use of frit-disc crucibles for routine and exploratory solution growth of single crystalline samples, Philos. Mag. **96**, 84 (2016).

[32] http://www.jcrystal.com/jcrystal.html.

[33] J. Zhang and S. Bobev, Synthesis, structural characterization and properties of $SrAl_{4-x}Ge_x$, $BaAl_{4-x}Ge_x$, and $EuAl_{4-x}Ge_x$ ($x = 0.3-0.4$)-Rare examples of electron-rich phases with the $BaAl_4$ structure type, J. Solid State Chem. **205**, 21 (2013).

[34] D. Martien, M. Williamsen, S. Spagna, R. Black, T. DaPron, T. Hogan, and D. Snow, An ultrasensitive differential capacitive dilatometer, IEEE Trans. Magn. **55**, 1 (2019).

[35] F. F. Balakirev, S. M. Ennaceur, R. J. Migliori, B. Maiorov, and A. Migliori, Resonant ultrasound spectroscopy: The essential toolbox, Rev. Sci. Instrum. **90**, 121401 (2019).

[36] O. Leupold, J. Pollmann, E. Gerdau, H. Rüter, G. Faigel, M. Tegze, G. Bortel, R. Rüffer, A. Chumakov, and A. Baron, Nuclear resonance scattering of synchrotron radiation at the 21.5 keV resonance of ^{151}Eu, Europhys. Lett. **35**, 671 (1996).

[37] V. G. Kohn, A. I. Chumakov, and R. Rüffer, Nuclear resonant inelastic absorption of synchrotron radiation in an anisotropic single crystal, Phys. Rev. B **58**, 8437 (1998).

[38] J. Y. Zhao, W. Bi, S. Sinogeikin, M. Y. Hu, E. E. Alp, X. C. Wang, C. Q. Jin, and J. F. Lin, A compact membrane-driven diamond anvil cell and cryostat system for nuclear resonant scattering at high pressure and low temperature, Rev. Sci. Instrum. **88**, 125109 (2017).

[39] W. Rehwald, The study of structural phase transitions by means of ultrasonic experiments, Adv. Phys. **22**, 721 (1973).

[40] F. R. Kroeger and C. A. Swenson, Absolute linear thermal-expansion measurements on copper and aluminum from 5 to 320 K, J. Appl. Phys. **48**, 853 (1977).

[41] R. Takagi, N. Matsuyama, V. Ukleev, L. Yu, J. S. White, S. Francoual, J. R. L. Mardegan, S. Hayami, H. Saito, K. Kaneko, K. Ohishi, Y. Ōnuki, T.-h. Arima, Y. Tokura, T. Nakajima, and S. Seki, Square and rhombic lattices of magnetic skyrmions in a centrosymmetric binary compound, Nat. Commun. **13**, 1472 (2022).

[42] http://energy.gov/downloads/doe-public-access-plan.

[43] D.-X. Chen, E. Pardo, and A. Sanchez, Demagnetizing factors of rectangular prisms and ellipsoids, IEEE Trans. Magn. **38**, 1742 (2002).

[44] E. Stryjewski and N. Giordano, Metamagnetism, Adv. Phys. **26**, 487 (1977).

[45] J. W. C. de Vries, R. C. Thiel, and K. H. J. Buschow, ^{151}Eu isomer shifts and charge transfer in Eu-base intermetallic compounds, Physica B+C **121**, 100 (1983).

[46] A. Chumakov and W. Sturhahn, Experimental aspects of inelastic nuclear resonance scattering, Hyperfine Interact. **123**, 781 (1999).

[47] V. Kohn and A. Chumakov, Dos: Evaluation of phonon density of states from nuclear resonant inelastic absorption, Hyperfine Interact. **125**, 205 (2000).

[48] I. Sergeev, Nisdos (private communication).

[49] A. Möchel, I. Sergueev, H.-C. Wille, F. Juranyi, H. Schober, W. Schweika, S. R. Brown, S. M. Kauzlarich, and R. P. Hermann, Lattice dynamics in the thermoelectric Zintl compound $Yb_{14}MnSb_{11}$, Phys. Rev. B **84**, 184303 (2011).